Scientific Report 2008

Institute for Energy Research-
Safety Research and Reactor Technology (IEF-6)

Safety Research for Nuclear Waste Disposal

Contents:

	page
Isotopic decontamination of neutron irradiated graphite ***D. Vulpius, M. Florjan, J. Fachinger***	**3**
Synthesis and properties of reaction-bonded SiC ceramic with embedded UO_2 - TRISO coated particles ***A.A. Bukaemskiy, J. Fachinger***	**5**
Selective separation of americium(III) from curium(III), californium(III), and lanthanides(III) by the LUCA process ***G. Modolo, P. Kluxen, A. Geist***	**11**
The crystallization of ThO_2-CeO_2 system ***A.A. Bukaemskiy, G. Modolo***	**15**
Layered double hydroxide containing Zr-IV ***H. Curtius, K. Ufer, K. Dardenne***	**19**
Adsorption of selenium on a Mg-Cd-Al layered double hydroxide ***B. Hansen, H. Curtius, R. Odoj***	**25**

Isotopic decontamination of neutron irradiated graphite

D. Vulpius, M. Florjan, J. Fachinger

Forschungszentrum Jülich GmbH, Institute for Energy Research, (IEF-6), D-52425 Jülich, Germany
Corresponding author: d.vulpius@fz-juelich.de

A method for removal of C-14 from irradiated nuclear graphite was developed. The method is based on the selective oxidation of C-14 whereby the graphite matrix remains widely unaffected. Consequently, it was concluded that C-14 in the graphite matrix is not present in the graphite lattice, but rather in a chemical form which is easier to oxidise compared to the C-12 of the graphite matrix. Presently an investigation of the chemical form and of the binding relations of C-14 is in progress.

Objectives

Worldwide more than 250,000 tons of irradiated graphite from nuclear reactors is under storage [1]. Detailed concepts for final disposal or reprocessing of this graphite do not exist up to now.

The main objective of the present work is to develop procedures for efficient decontamination of used reactor graphite, e.g. the separation of C-14 from the graphite matrix by thermal treatment (partial oxidation). A successful separation could reduce the radiotoxicity of the graphite waste and offer a more favourable disposal strategy.

Furthermore, it is planed to develop a closed nuclear graphite cycle. Overall, the recovery of irradiated graphite for new nuclear applications and the separation of C-14 as resource material for scientific and commercial uses would be highly desirable.

Introduction

Nuclear graphite is a polycrystalline and porous material. In its pore system gases and liquids can adsorb. Additionally during production of reactor graphite heterocyclic compounds containing nitrogen are used to bind the graphite crystallites. The mayor process to create C-14 in graphite during neutron irradiation in the reactor is the $^{14}N(n,p)^{14}C$ reaction with a cross section of 77 mb. The recoil energy of the hot C-14 atom is 40 keV [2] much higher than any chemical bond, hence, the C-14 will be substantially displaced from its origin.

Experiments

The thermal treatment of irradiated graphite samples from the decommissioned nuclear reactors AVR and MERLIN at Jülich was carried out in a laboratory furnace at temperatures between 900 °C and 1300 °C. Nitrogen was used as carrier gas. The carrier gas contained either oxygen (max. 1.2 vol.-%) or water steam as oxidising agents. The duration of the treatment amounted to 3 hours for oxygen and to 7 hours for water steam. The flue gas was washed in 0.1 M HNO_3 and in 4.0 M NaOH to absorb H-3 and C-14, respectively. The content of H-3 and C-14 was measured with liquid scintillation counting. The experimental set-up for the thermal treatment is outlined in Fig. 1.

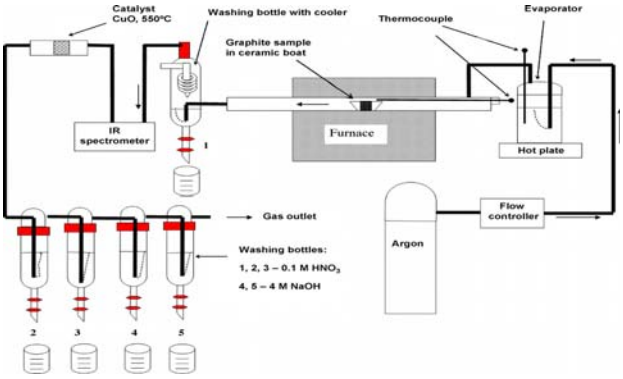

Fig. 1: Experimental set-up for the thermal treatment

Results and discussion

Our results [3] demonstrate that the main part of the C-14 inventory can be removed from the graphite matrix by selective oxidation. In oxygen a C-14 release of maximum 79 % with a mass loss of the matrix of 2.9 % within 3 hours was determined. In water steam a C-14 release of maximum 93 % with a mass loss of the matrix of 5.4 % within 7 hours could be detected. Fig. 2 and Fig. 3 show the corresponding graphs.

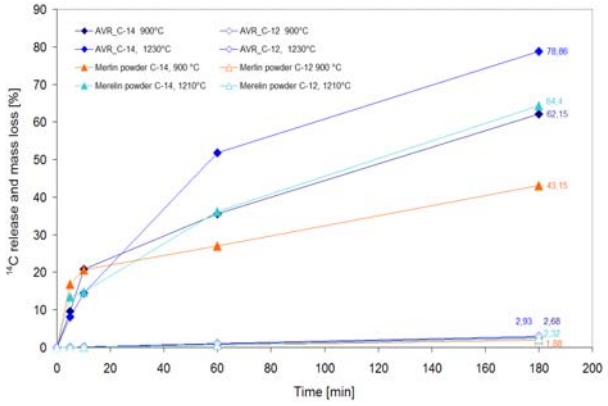

Fig. 2: Release of C-14 in oxygen (max. 1.2 vol.-%)

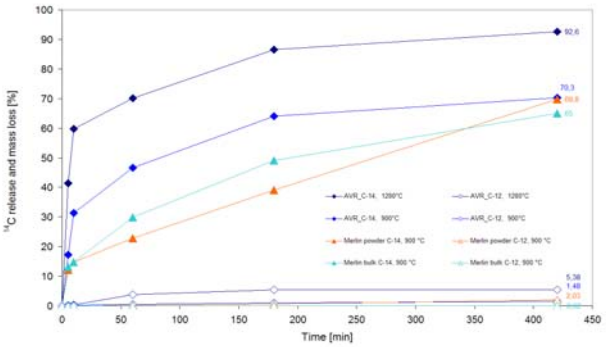

Fig. 3: Release of C-14 in water steam

In view of the equality of chemical behaviour of isotopes (in this case C-12 and C-14) these results lead to the question: Why C-14 can be easier oxidised compared to C-12 from the same material? We conclude that the C-14 is not integral part of the graphite lattice, but it is attached to the surface of the graphite crystallites or loosely adsorbed between the graphite lattice planes. These suppositions have to be investigated by future experimental work.

Outlook

A systematic spectroscopic study to understand the chemical bonding of C-14 in irradiated graphite is under way. At the moment investigations are carried out using Raman spectroscopy, secondary ion mass spectroscopy and X-ray photoelectron spectroscopy. Possibly, ion implantation experiments and neutron irradiation experiments will be necessary to simulate the formation of C-14 in a nuclear reactor and to increase the amount of C-14 in the graphite samples for spectroscopic analysis. These studies should help to optimise the decontamination process and to develop new decontamination methods.

In addition, we want to transfer our laboratory experiments into a half-technical grade. For this purpose we have purchased an induction furnace to obtain temperatures up to 2500 °C coupled to a mass spectrometer for the analysis of the flue gases. Furthermore, we want to extend the method for decontamination of radioactive metal nuclides (e.g. Fe-55, Co-60, Ni-63 and Cs-137) by converting them to their volatile chlorides at temperatures higher than 1500 °C.

The first test run with the new furnace is shown in Fig. 4 using a non-irradiated AVR graphite pebble at 1000 °C.

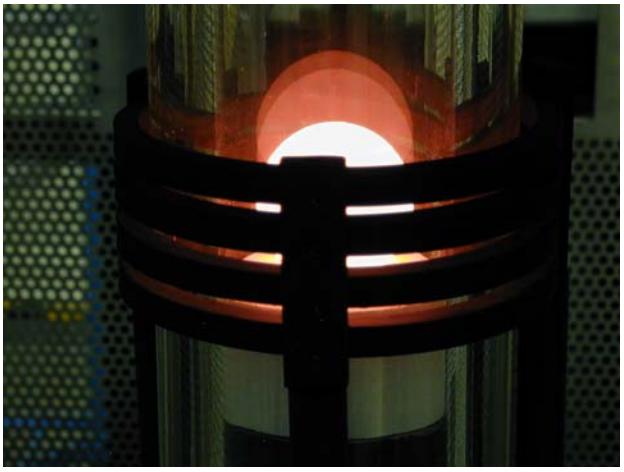

Fig. 4: AVR graphite pebble at 1000 °C

Acknowledgement

This work is supported by the European Commission (project CARBOWASTE, contract no. FP7-211333).

References

[1] European Commission, Seventh Framework Programme, *CARBOWASTE. Treatment and disposal of irradiated graphite and other carbonaceous waste*, Annex I – "Description of work".

[2] R. D. Finn, H. J. Ache, A. P. Wolf, *Chemical effects following $^{14}N(n,p)^{14}C$ in magnesium nitride*, J. Phys. Chem. 73 (1969) 3928-3933.

[3] M. Florjan, *Dekontamination von Nukleargraphit durch thermische Behandlung*, PhD thesis, Rheinisch-Westfälische Technische Hochschule Aachen, 2009.

Synthesis and properties of reaction-bonded SiC ceramic with embedded UO_2 - TRISO coated particles

A.A. Bukaemskiy, J. Fachinger

Forschungszentrum Jülich GmbH, Institute for Energy Research, (IEF-6),D-52425 Jülich, Germany
Corresponding author : a.bukaemskiy@fz-juelich.de

The disposal of spent HTR fuel elements requires a relatively large volume due to the integration of fuel particles and moderator graphite. This can be reduced by separating the coated particles from the graphite matrix. However, the coated particles cannot be disposed without a suitable embedding or backfill. In the Institute of Energy Research (IEF-6, Safety Research and Reactor Technology), the development of the advanced material for the nuclear waste disposal is one of the foreground task. In the framework of this task, SiC ceramic are considered as a possible long-term stable matrix for radioactive waste proposed for final disposal. SiC-base ceramic with the embedded the UO_2 - TRISO coated particles (CP) was synthesized by the reaction-bonding process and physic-mechanical properties of the synthesized samples were investigated.

Objectives

The direct disposal of spent HTR fuel element pebbles includes the disposal of more than 90 vol.% graphite, which contains only a low level of short- and long-lived radioactive contamination whereas the coated particles may be considered as high-level waste (HLW). The disposal of the coated fuel particles separated from the graphite matrix will reduce the required storage volume, significantly. However, the coated particles cannot be disposed as bulk good without a backfill to ensure their long-time safety at the geological disposal.

Silicon carbide (SiC) is a prevalent material for many technological applications because of its high mechanical, chemical and thermomechanical properties. Ceramics based on SiC are characterized by extreme hardness, high thermal conductivity, relatively low thermal expansion, small porosity and chemical durability [1]. In general, SiC is not thermodynamically stable in oxidizing environments, but the stable SiO_2 layer formed by oxidation largely passivates the surface and prevents further corrosion [2, 3]. In principle, SiC ceramics can be considered as a long-term stable matrix for radioactive waste proposed for final disposal. The most suitable option for spent HTR fuel incorporation is the reaction-bonded silicon carbide (RBSiC), which is produced by infiltration of SiC/C-green bodies with molten Si. The advantage of RBSiC is the little or no shrinkage of the composite, so near-net shaped green bodies can be produced [4].

In present work, the reaction-bonded silicon carbide ceramic with embedded UO_2 - TRISO coated particles was produced. The physic-mechanical properties, such as microstructure, coated particles packing group, Vickers microhardness, and fracture toughness of synthesized samples were investigated in detail. The strength properties, such as tensile strength of synthesized samples, failure mechanism, microstructure of the fracture surface, and the peculiarities of the coated particles fracture were also studied.

Results

Silicon powder (mixes of the coarse (44 μm) and fine SiC (2μm) particles) and Graphite flakes were used as initial materials. The powders were consequently mixed for 3 hours in the ball mill. The slip with powders load 37.5 wt.% was produced by weighing the appropriate amounts of NaOH (pH ~ 10 – 11) followed by thorough mixing. Slip was then mixed with of UO_2 - TRISO coated particles in the ratio 2/1 by weight. This mixture was subsequently filtered in a device specially designed for this purpose and placed in a standard SiC crucible (Wacker Ceramics, inner diameter – 10 mm, outer diameter – 20 mm, height – 25 mm). Silicon powder was added above the green compacts in the crucible. Then, the samples were reaction bonded in the oven under vacuum at 1600°C (0.5 hour).

In the present work, the UO_2 - TRISO coated particles were used. These CP consist of the UO_2 fuel kernel surrounded sequentially by a porous pyrocarbon buffer, inner pyrocarbon layer (IPyC), SiC layer and outer pyrocarbon layer (OPyC), as shown in Fig.1.

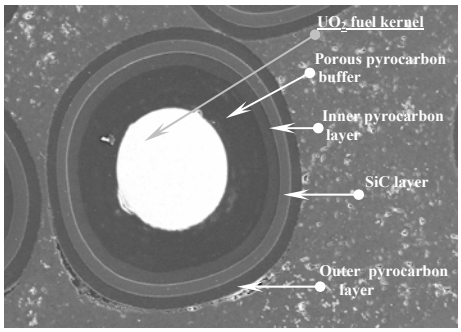

Fig. 1. SEM photograph of UO_2 - TRISO coated particles

The main characteristics of the UO_2 - TRISO coated particles are summarized in Table 1. Our values of the coating thickness are in agreement with the literature data on TRISO particles [5].

Table 1.

Coated particle mass m_{CP}, mg	1.35
Coated particle diameter d_{CP}, μm	890
UO_2 fuel kernel diameter, μm	500
Porous pyrocarbon buffer, μm	90
Inner pyrocarbon layer (IPyC), μm	35
SiC layer, μm	30
Outer pyrocarbon layer (OPyC), μm	40

Several test samples were cut up by the samples height (Fig. 2 a) and polished by diamond pastes for the following investigation (Fig. 2 b). As evident from Fig. 2 b, the distribution of the coated particles in the RBSiC matrix seems largely homogeneous; the quantity of the pores is insignificantly.

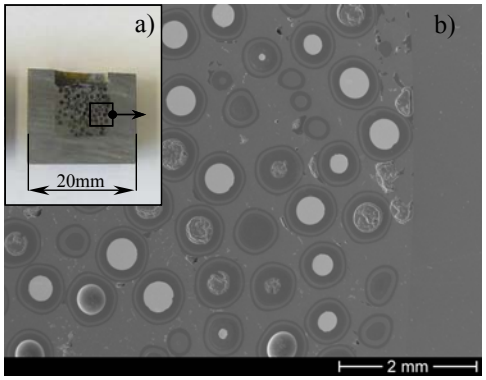

Fig. 2. Test samples section (a) and SEM photograph of synthesized ceramic (b)

Fig. 2 b shows the good quality of the junction between CP and RBSiC matrix and between RBSiC matrix and the SiC crucible. The failure of the coated particles was not observed. It is necessary to note that a comparison of sample height of the green body before and after reaction bonding does not reveal any valuable dimension changes. This shows that near-net shape production is possible via reaction bonding.

The packing of the UO_2 - TRISO coated particles in the specific SiC crucible was experimentally studied, and the numerical simulation was also used [6]. For the representative case shown in Fig. 2 b, the density of the coated particles in RBSiC matrix equals 38.13 vol.%. The SEM investigations of polished and fracture surfaces of RBSiC + CP ceramic are attested that the CP have a tendency to form the layering of the CP in RBSiC matrix with periodicity about 1 mm, Fig. 2 b. The distance between apparent centers of adjacent CP and outer diameters of the SiC layer were measured from SEM photographs for the twenty couple of the coated particles. The correction for position of CP center over or under sample surface was performed using known outer diameter of the SiC layer (810 μm), Table 1. The average distance between centers of CP equals 980 ± 60 μm that corresponds the thickness of intermediate RBSiC layer between coated particles in 90 μm. The comparison of the results of the numerical simulation with the experimentally measured value of the tap density and the results of the SEM investigations allow to assume that in case of the RBSiC + CP ceramic the orthorhombic packing type of the coated particles with the attached thin RBSiC layer takes place.

The values of micro hardness (*Hv*) and fracture toughness (K_{1C}) were measured for all four ceramic components of the synthesized samples. In case of the coated particles, there are UO_2-kernels and SiC-layer, for the SiC-ceramic – SiC crucible wall and synthesized RBSiC. The typical SEM photograph of the sample surface prepared for the measurements is shown in Fig. 3. The values of Hv and K_{1C} are calculated by average values of ten measurements and summarized in Table 2.

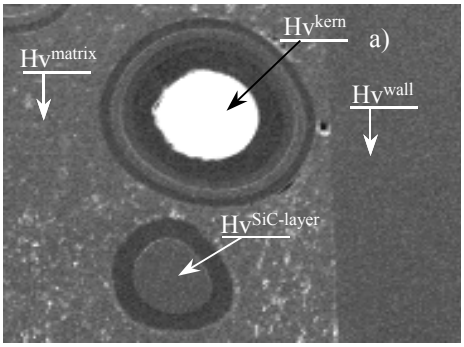

Fig. 3. Typical SEM photographs of samples surface with typical points for indenting.

Table 2

Material	*Hv*, GPa	K_{1C}, MPa·m$^{0.5}$
UO_2-Kernel	7.1 ± 0.4	0.9 ± 0.1
SiC-layer	34 ± 2	2.3 ± 0.2
RBSiC-matrix	26 ± 2	3.0 ± 0.5
SiC-wall	36 ± 2	3.2 ± 0.3

The kernel has high-density structure with small quantity of the pores. The values of Hv and K_{1C} have good agreement with literature data (*Hv* = 6 – 7 GPa; K_{1C} = 0.9 – 1.1 MPa m$^{0.5}$ [7, 8, 9]).

The SiC layer has the high-density structure too, what determines high value of the microhardness . However, the value of K_{1C} = 2.3 ± 0.2 MPa m$^{0.5}$ is less then that reported in the reference data (*Hv* = 33 – 38 GPa; K_{1C} = 3 -3.5 MPa m$^{0.5}$ [10, 11]). This fact may be caused by the geometrical factor, because the indentation of thin SiC layer takes placed. In our case, the thickness of SiC layer (~ 30 μm) is comparable with the average length of the crack, which equals ~ 22 μm.

SiC crucible wall has the high-density structure with small quantity of the pores and the values of *Hv* and K_{1C} very high and have a good agreement with literature data [10, 11].

In case of RBSiC-matrix, the value of *Hv* is in 1.4 times less then for SiC crucible wall, but this correlates with the reference date for Reaction-Bonded SiC ceramic (*Hv* = 21 - 34 GPa; K_{1C} = 3.6 – 4.2 MPa $m^{0.5}$ [12, 13]).

The diametral compression test (Brasilian Test) [14, 15, 16] was used for the measurements of the tensile strength of the synthesized ceramics. The Brasilian test is based on the state of stress development when a cylindrical specimen is compressed between two diametrically opposite plates (Fig. 4 a). The Brasilian disk test was originally designed to determine the mechanical properties of the concrete and rock material [14], later the test was successfully used for glass and ceramics [15, 16], including the nuclear waste materials [17].

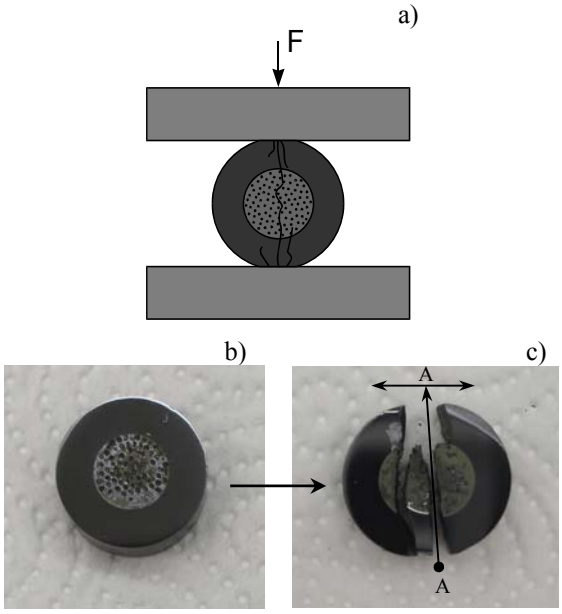

Fig. 4. Schematic representation Diametral Compression Test (a), RBSiC + CP - SiC samples before (b) and after (c) test.

The tensile strength (σ_t) was calculated as average of 3 - 5 measurements. The initial samples are the reaction-bonding SiC ceramic with embedded UO_2 - TRISO coated particles (RBSiC + CP ceramic) cased in the SiC crucible. The samples are cut horizontally into cylinders and their surfaces are grinded and carefully polished using diamond paste (1μm). Thus, two types of the samples were prepared for the testing, namely the flat cylinder consisting of the synthesized RBSiC + CP ceramics is surrounded by the layer of the SiC crucible (middle part of the initial sample) and, as a control sample, a cylinder from pure SiC of the crucible (bottom of the initial sample). For these samples the notifications RBSiC + CP - SiC – Disk, SiC – Disk, correspondingly will be used below.

The typical photos of RBSiC + CP - SiC – Disk sample before and after testing is shown in Figs. 4 b, c correspondingly. As usual, during the Brasilian test the explosive pattern of the failure was observed. In addition to the coarse fragments shown in Figs. 4 c the broken samples contain also some quantity of the small thin flake fragments. In cases of RBSiC + CP - SiC – Disk and SiC – Disk, the typical fracture pattern was triple-cleft with varying degrees of the fragmentation [17, 18]. This fracture mechanism was schematically shown in Fig. 4 a. This fracture mechanism is typically for the high-modulus, high-strength ceramics.

The value of the tensile stress for the SiC – Disk (σ_t = 200 ± 35 MPa) has good agreement with the references date (σ_t = 214 ± 55 MPa [19]). In case of the synthesized ceramic (RBSiC + CP - SiC – Disk) the value of σ_t equals 17 ± 3 MPa and this is twelve times less than the corresponding value for the SiC - Disk. The low value of σ_t for the RBSiC + CP ceramic is apparently determined by the presence of a large amount of CP in RBSiC matrix. The CP may be considered as the large porous. The total volume of the CP in RBSiC matrix equals to 38 vol. %. The influence of porosity (*P*) on the strength characteristics of ceramics was studied in detail in [20]. In case of SiC ceramic, the tensile strength dependence on porosity can be described as $\sigma_t/\sigma_t^o \sim exp(-bP)$, where σ_t is the tensile stress of the height density ceramic, b – empirical coefficient (for SiC b = 4.5 [21]). This equation predicts the decrease of the tensile strength of RBSiC + CP ceramics in 5.5 times. Moreover, the tensile strength is the microstructure sensitive parameter and depends strongly on porous size [20]. For examples, the value of σ_t decreased on order of magnitude at increasing of the pore size in 5 – 7 times [20]. In our case, coated particles may be considered as the big porous. Apparently, the strength of the synthesized samples (reaction-bonding SiC ceramic with embedded UO_2 - TRISO coated particles cased in the SiC crucible) is mainly determined by the strength of protective device (SiC crucible). These conclusions are valid for the particular samples geometry used in the present study. For the more accurate conclusions, the realization of the additional theoretical and experimental investigations is necessary.

At the study of fraction mechanism of the synthesized samples, three important aspects should be investigated in detail, namely, a) microstructure of the junction between synthesized RBSiC ceramic and SiC container; b) microstructure and fracture of the synthesized RBSiC matrix and c) the fracture of the coated particles. For all investigated samples, the failure surface nearly the boundary between RBSiC + CP and SiC ceramic is smooth and the exfoliation of the material is not observed, Fig. 5 a. It confirms high performance of the junction between synthesized RBSiC ceramic and SiC container. Fig. 5 a shows good junction between synthesized RBSiC + CP ceramic and SiC container takes place throughout the interface.

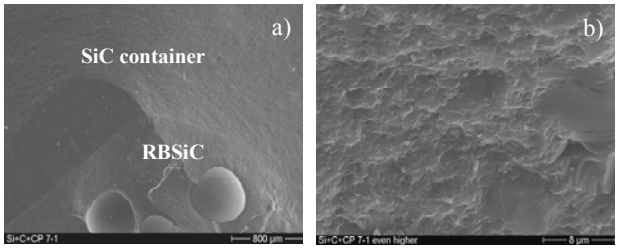

Fig. 5. Representative SEM photographs of (a) fracture surfaces in region of of the junction between synthesized RBSiC ceramic and SiC container and of (b) RBSiC ceramic fracture surfaces.

The fracture surfaces of RBSiC matrix are shown in Fig. 5 b. The character of fracture is typical for the brittle ceramic. The transgranular mechanism of material fracture is observed, i.e. the failure of the ceramic mainly takes place across grains and not by grain boundaries [22].

For the study of the fracture mechanism of the coated particles, the sample shown in Fig. 4 c was investigated after Brasilian fracture test in detail. The broken sample consists of three large fragments, which are shown in Fig. 4 c and eighteen small thin flake fragments with the size about few millimetres.

The mating surfaces shown in Fig. 4 c as A-A plane were investigated in detail. For each cleavage surface the mating coated particles were found and numbered. For each coated particle the type of the failure and the conservation of the kernel in ceramic matrix were studied.
There is no doubt that the failure of the coated particles has complex character, but in ideal case, the possible failure surfaces of the TRISO CP are next:
a) surface between outer pyrocarbon layer (OPyC) and RBSiC ceramic matrix;
b) surface between SiC and outer pyrocarbon layers;
c) surface between inner pyrocarbon (IPyC) and SiC layers;
d) surface between porous pyrocarbon buffer and inner pyrocarbon layer;
e) surface between kernel and porous pyrocarbon buffer.

SEM photographs of the broken coated particles N1 and N6 located on the left (Fig. 6 a) and the right (Fig. 6 b) side of the cleavage surface are shown in Fig. 6 c, d and Fig. 6 e, f correspondently. In first case, the CP N1 breaking takes place by the surface between kernel and porous pyrocarbon buffer, in second case – by the surface between SiC and outer pyrocarbon layers.

In addition to cases demonstrated in Fig. 6 c-f, the examples of the CP failure by the surface between porous pyrocarbon buffer and inner pyrocarbon layer and by the surface between inner pyrocarbon (IPyC) and SiC layers are shown in Fig. 6 g, h, correspondingly. It is necessary to note that these variants of CP failure occur sufficiently rarely than the failure by the Kernel – Buffer and SiC layer – OPyC surfaces and take place mainly at the periphery of the fragments.

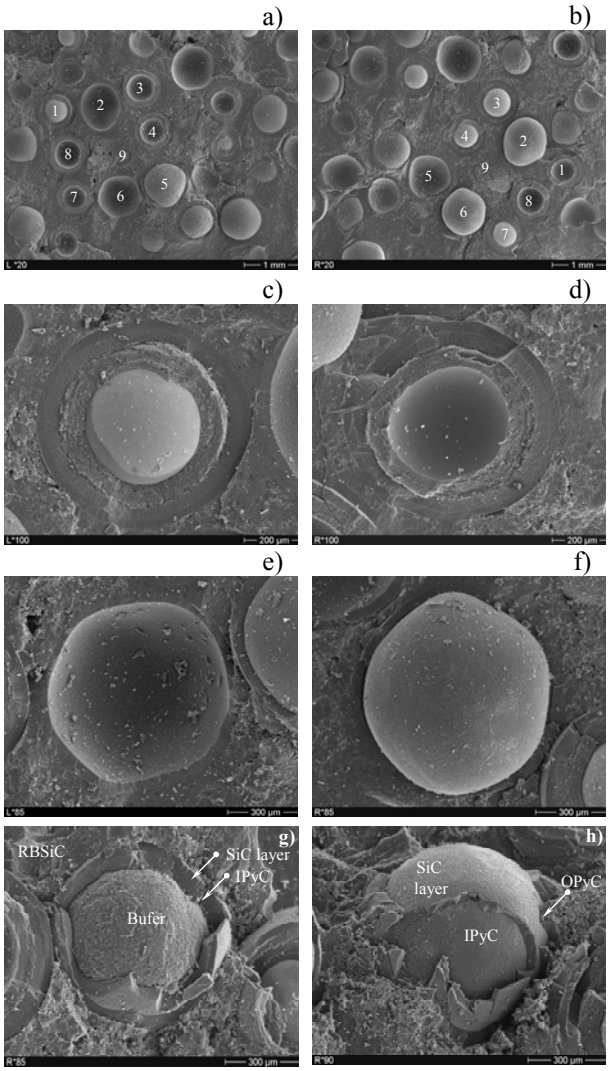

Fig. 6. Representative SEM photographs of left (a) and right (b) side of cleavage surface (fragment), of broken coated particles (c, d) N1 and (e, f) N6 located on left and right side of cleavage surface and of CP failure by surface between (g) Buffer – IpyC and (h) IpyC - SiC layers.

The results of the investigation of both sides of the fragment cleavage surface are summarized in Table 3. In addition to information about the type of the failure of the coated particles (column "Fracture surface") and the conservation of the kernel in ceramic matrix (line "Absent kernels"), the disposition of CP on the plain or periphery part of the fragment (columns "Plain" and "Periphery", correspondingly) was studied. Full number of the processed CP equals seventy-two, which is approximately 30 % from total number of CP in the full failure surface (*Ns* = 250 st.).

Table 3.

Fracture surface	Amount		Plane		Periphery	
	N	N, %	N	N, %	N	N, %
SiC layer - OPyC	33	46	31	61	2	10
Kernel-Buffer	28	39	13	25	15	71
Buffer – IPyC	8	11	4	8	4	19
IPyC – SiC layer	3	4	3	6	--	--
Sum	72	100	51	100	21	100
Absent kernels	9	12.5	4	8	5	24

The number of the absent kernel equals nine, which is 12.5 % from the full number of the processed CP (72 st.). The kernels and coated particles break off mainly from the periphery part of the fragments (24 %), while from the plain part of the fragment – 8 % only.

The failure of the coated particles meanly takes place by the surface between SiC and outer pyrocarbon layers (46 %), by the surface between kernel and porous pyrocarbon buffer (39 %). However, the probability of the CP failure by these surfaces for the plain and periphery part of the fragment differs drastically. In case of the plain part of the fragment, the failure of the coated particles occurs mainly by the surface between SiC and outer pyrocarbon layers (61 %), while on the periphery part – only 10 %. And vice versa, in case of the periphery part of the fragment the failure of the coated particles occurs mainly by the surface between kernel and porous pyrocarbon buffer (71 %), while on the plain part – only 25 %. The probability of the CP failure by other surfaces (Buffer – IPyC and IPyC – SiC layer) is not large and amounts to 14 and 19 % for the plain and periphery part of the fragment, correspondingly. The CP failure by the surface between outer pyrocarbon layer (OPyC) and RBSiC ceramic matrix was not found.

The CP failure by the surface between SiC and outer pyrocarbon layers is preferable from the safety standpoint; since in this case the radioactive kernels are defended against the environment by the outer SiC cover.
The reasons of CP failure by the surface between SiC and outer pyrocarbon layers or by other surfaces were studied in detail. The image and EDX analysis of a lot of the broken coated particles show that two type of the CP state are presented in the synthesized RBSiC + CP ceramic.
In the first case, all covering layers of the TRISO coated particle are presented, the representative example of this type CP failure is shown in Fig. 7 a. The presence of the "soft" outer pyrocarbon layer results in the failure of coated particle by the surface between SiC and OPyC layers. Apparently, the "soft" outer pyrocarbon layer operates as the shock absorber (buffer), what in the presence of the strong SiC covering layer allows keeping intact of the CP at the material failure.

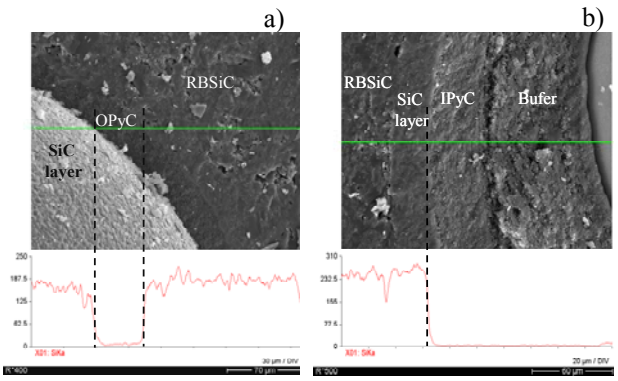

Fig. 7. Representative SEM photographs of broken coated particles and EDX analysis for Si content for the failure of CP by (a) surface between SiC and outer pyrocarbon layers and by (b) surface between kernel and porous pyrocarbon buffer.

In second case, the outer pyrocarbon layer of the TRISO coated particle is absent, apparently as a result of its reaction with the molten silicon during RB synthesis. The representative example of this type CP failure is shown in Fig. 7 b. The boundary of RBSiC matrix extends directly to SiC covering layer of CP, which is clearly demonstrated on the base of the results of EDX analysis. Apparently, the good junction between synthesized RBSiC matrix and SiC layer of CP takes place. Therefore, the breaking of SiC covering layer of CP with the post breaking of comparatively "soft" IPyC and buffer layers up to the kernel also occurs at material failure.

As was described above, the strength properties of the synthesized RBSiC + CP ceramic are meanly determined by the porosity of ceramic. In second case (OPyC layer is absent), the effective coated particle diameter d_{CP} decreases up to the diameter of IPyC layer, i.e. from 890 to 750 μm. The porosity of the synthesized RBSiC + CP ceramic decreased from 38.1 to 22.8 %, which should be resulted in increasing of strength properties by a factor of two. However in this case, the failure of the synthesized RBSiC + CP ceramic is mainly accompanied by the breaking of all covering layer of coated particles up to kernels, which is not desirable from the safety standpoint. On the other hand, in first case (all covering layers are presented), the effective coated particle diameter d_{CP} decreases lightly. But in this case, the CP failure by the surface between SiC and outer pyrocarbon layers mainly take places, that is preferable from the safety standpoint; since in this case the radioactive kernels are partially defended against the environment by the outer SiC cover. The production of RBSiC + CP ceramic with the optimal mechanical and safety properties should be the object of the following investigations.

Summary

In present work, SiC ceramic was considered as a possible long-term stable matrix for radioactive waste proposed for final disposal. The SiC-base ceramic with the included UO_2 - TRISO coated particles was synthesized by a reaction-bonding process.

At the study of the sample's microstructure, it was shown that the distribution of the coated particles in the RBSiC matrix is homogeneous; the CP have a tendency to form the layering in RBSiC matrix with the orthorhombic packing type; the content of the coated particles in RBSiC matrix equals 38,1 %; the quantity of the pores is insignificantly; the good quality of the junction between CP and RBSiC matrix and between RBSiC matrix and the SiC crucible take place; the crippling of the coated particles is not observed.

For all ceramic components of the synthesized samples, namely, for the UO_2-kernels, coated particles SiC-layer, SiC crucible wall and for the synthesized RBSiC, the values of micro hardness (*Hv*) and fracture toughness (K_{1C}) were measured, analyzed and compared with the reference data.

The synthesized ceramic (RBSiC + CP - SiC – Disk) is characterized by the value of σ_t equals 17 ± 3 MPa. The influence of porosity (*P*) on the strength characteristics of the synthesized ceramics was considered. It was shown that the strength of the synthesized samples is mainly determined by the strength of protective device (SiC crucible).

At the study of fraction mechanism of the synthesized samples, It was shown that the good junction between synthesized RBSiC + CP ceramic and SiC container takes place throughout the interface. The transgranular mechanism of material fracture of the reaction-bonded SiC ceramic was observed.

The failure of the coated particles mainly takes place by the surface between SiC and outer pyrocarbon layers and by the surface between kernel and porous pyrocarbon buffer. The reasons of CP failure by the surface between SiC and outer pyrocarbon layers or by other surfaces were studied in detail.

References

1. Snead L.L., Nozawa T., Katoh Y., Byun T., Kondo S., Petti D. J.Nucl.Mat., 2007. 371. 329-377.
2. Kriegesmann J. *Herstellung und Eigenschaften von Siliciumcarbidkeramiken.* Technische Keramik, 1990. 40–51.
3. Li R. *Temperature-induced direct casting of SiC.* Bericht Nr.102, Dissertation, Max-Planck-Institut für Metallforschung, Stuttgart. 2001.
4. Richerson D.W. *Modern Ceramic Enginering.* Marcel Dekker, Inc. 1992.
5. Nickel H., Nabielek H., Pott G., Mehner A.W. Nucl.Eng.Des., 2002. 217. 141-151.
6. Mueller G.E. Pow. Tech., 2005. 159. 105-110.
7. Vollath D., *Uranium Dioxide, UO2, physical properties.* Gmelin Handbook of Inorganic Chemistry, Suppl. V. C5, Springer Verlag, 1986. 8-12.
8. Yamada K., Yamanaka S., Katsura M. J.Alloy.Comp., 1998. 271-273. 697-701.
9. Matzke H., Inoue T., Warren R. J.Nucl.Mat., 1980. 91. 205-220.
10. Niihara K. Ceram. Bull., 1984. 63, 9. 1160-1164.
11. Motojima S., Iwamori N. J. Mat.Scien. 1986. 21. 1363-1367.
12. Yamaguchi T. et al. *Engineering ceramics*, Tokyo, Japan: Gihodoshuppan, 1984.
13. Tanaka S., Sugimoto S., Li J., Watanabe R., Esashi M. J. Microelectromech. Sus., 2001. 10, 1. 55-61.
14. Carneiro F.L.L.B., Barcellos A. Instituto Nacional de Technologia. Rio de Janeiro, 1949.
15. Brückner A., Fett T., Munz D., Schirmer K. J. Eur.Ceram.Soc., 1997. 17. 689-696.
16. Spriggs R.M., Brissette L.A., Vasilos T. Mater. Res. Stand. 1964, 4, 5. 218-220.
17. Marion R.H., Johnstone J.K. Ceram. Bull. 1977. 56, 11. 998-1002.
18. Petroski H.J., Ojdrovic R.P. Int. J. of Fract. 1987. 34. 263-279.
19. Yu R.C., Ruiz G., Pandolfi A. Eng. Frac. Mech. 2004. 71. 897-911.
20. R.W. Rice. *Porosity of ceramics,* Marcel Dekker, Inc., New York, 1998.
21. Seshadri S.G., Srinivasan M., Chia K.Y., Am. Cer. Soc. Westerville, OH, 1989.
22. *Fracture an advanced treatise. V7 Fracture of nonmetal and composites*. Ed. H. Liebowitz. Academic press, New York, 1972.

Selective separation of americium(III) from curium(III), californium(III), and lanthanides(III) by the LUCA process

G. Modolo[1], P. Kluxen[1], A. Geist[2]

[1]*Forschungszentrum Jülich GmbH, Institute for Energy Research,(IEF-6), 52425 Jülich, Germany*
[2]*Forschungszentrum Karlsruhe GmbH, Institut für Nukleare Entsorgung, 76021 Karlsruhe, Germany*

Corresponding author:g.modolo@fz-juelich.de

The LUCA process was developed at Forschungszentrum Jülich for the selective separation of Am(III) from an acidic solution containing the trivalent actinides Am(III), Cm(III), and Cf(III) as well as lanthanides. A mixture of 0.4 mol/L bis(chlorophenyl)dithiophosphinic acid and 0.15 mol/L tris(2-ethylhexyl)phosphate dissolved in 20 % isooctane / 80 % tert.-butyl benzene was used as the extractant. The process was carried out in centrifugal contactors using an optimized flowsheet involving 7 stages for extraction, 9 stages for scrubbing and 8 stages for back-extraction. Very encouraging results were obtained. A high feed decontamination factor was obtained for Am(III) (> 1000), and recovery in the product after stripping was higher than 99.8 %. The Am(III) product was contaminated with 0.47 % Cm(III). More than 99.9 % Cf(III), Eu(III) and > 99.5 % Cm(III) inventories were directed to the raffinate and the contamination with Am(III) (< 0.08%) was low. The experimental results were in good agreement with the predictions of a computer code

Introduction

During the last decade a large amount of research has been conducted in several countries on the separation and recovery of Am and Cm from the high-level liquid waste (HLLW) fraction of the PUREX process. A comprehensive survey on actinide separation science and technology is given by Nash et al. [1]. Most partitioning strategies rely on the following separation processes.

1. Separation of uranium and/or plutonium from spent fuel dissolution liquors (e.g. PUREX, UREX)
2. Co-extraction of the trivalent actinides and lanthanides (e.g. TRUEX, DIAMEX, TRPO, TODGA)
3. Separation of trivalent actinides from lanthanides (e.g. TALSPEAK, SANEX)

The last step is important because it is essential to separate americium and curium from trivalent lanthanides to avoid the strong absorption of thermalized neutrons by the lanthanides, particularly if the trivalent actinides are to be recycled as fuel (or targets for transmutation) in a current generation reactor. Due to similarities in the chemical properties and behaviour of trivalent actinides and lanthanides, extractants or complexing agents containing soft donor atoms such as N, S, Cl, etc. are required for reliable group separations [1-3]. After the An(III)/Ln(III) separation process, the product fraction contains approx. 0.35 to 0.45 g/L Am and Cm (e.g. after a BTBP process [4]).

In principal, both elements could be transmuted together in a fast reactor or ADS system. However, because of the high heat decay and neutron emission of curium, any dry or wet fabrication process will require remote handling and continuous cooling in hot cells behind thick concrete shielding. The development of a simple, compact and robust fabrication process appears to be a great challenge [5]. One option involves the interim storage of curium for about 100 years, after which the relatively short-lived curium isotopes (^{242}Cm, ^{243}Cm, and ^{244}Cm) decay to plutonium isotopes which can then be easily separated from americium. Therefore, an effective method for separating Am from Cm prior to re-fabrication is a major prerequisite for the discussion of further fuel cycle scenarios.

The separation of adjacent trivalent actinides represents an even more challenging task than the An(III)/Ln(III) separation. It is known that the separation of americium from curium is a very difficult operation, due to the very similar properties of these elements. Numerous techniques, including high-pressure ion exchange, extraction chromatography, and solvent extraction using e.g. di(2-ethylhexyl)phosphoric acid (HDEHP) have been used for Am(III)/Cm(III) separation and purification [1]. However, the Am/Cm separation factors were low and do not exceed 3, necessitating a large number of stages in order to obtain a pure product.

The best separation of transplutonium elements has been obtained using methods based on the various oxidation states of the separated elements. Contrary to Cm, Am can be oxidized in aqueous solutions to oxidation states higher than III, i.e. IV, V and VI. Nevertheless, these Am oxidation states are thermodynamically unstable in acidic aqueous solutions. The solvent extraction of hexavalent Am has been studied by several authors [6, 7].

In-depth experience has been gained at CEA over the last 20 years, and several SESAME tests have been carried out in Marcoule, France [8]. Although the results of the tests were encouraging, the process was nevertheless not sufficiently robust for further industrialisation. The CEA is now considering the development of a novel option for Am/Cm separation based on the difference of the affinity of the DIAMEX extractant (DMDOHEMA) for Am(III) and Cm(III) [9-10]. Since the Am(III)/Cm(III) separation factor of 1.6 is low, this process requires a large number of stages.

The synergistic mixture (Figure 1) composed of bis(chlorophenyl)dithiophosphinic acid [$(ClPh)_2PSSH$] and tris(2-ethylhexyl)phosphate (TEHP) shows a very high affinity for actinides(III) over lanthanides(III). Am(III)/Eu(III) separation factors is over 3000. Surprisingly high Am(III)/Cm(III) separation factors of 6–10 were also reported by Modolo et al [11]. Based on the extraordinary extraction properties of the above synergistic mixture, the LUCA process [12] was invented. LUCA is the acronym for "**L**anthaniden **U**nd **C**urium **A**mericum separation". The present paper relates to the development and demonstration of a continuous LUCA process for the selective recovery of Am(III) from an aqueous nitric acid solution containing trivalent actinides (i.e. Am(III), Cm(III) and Cf(III)) and trivalent lanthanides. Optimisation studies were carried out to define the best conditions for extraction, scrubbing and stripping. In addition to the batch extraction studies, a single-stage extraction experiment was conducted to obtain more data on the system kinetics, and to generate data required for the flowsheet calculations. After the data was collected, a 24-stage flowsheet was designed, and the final assessment was performed in a counter-current test using miniature centrifugal contactors [13].

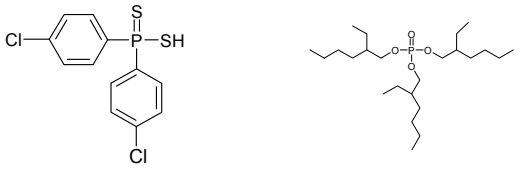

Fig.1: Synergistic mixture of $(ClPh)_2PSSH$ and TEHP used in the LUCA process

Flowsheet design

Extensive batch extraction studies were carried out at Jülich as the basis for the development of continuous counter-current spiked tests devoted to the selective separation of Am(III) from Cm(III) using a "$(ClPh)_2PSSH$ /TEHP" mixture. To calculate a flowsheet for the separation test, a computer code similar to codes used for mass transfer calculations in hollow fibre modules [14-16] was established at Forschungszentrum Karlsruhe (INE).

With these data, a flowsheet was calculated to achieve approx. 0.1 % Am(III) in the raffinate and approx. 2 % Cm(III) in the product (of course, the product is even better decontaminated from metal ions less-extracted than Cm(III), i.e. Cf(III) and Eu(III), which is the reason why they were not included in the calculations). The major constraint was that 16 stages were available for extraction and scrubbing. The proposed flowsheet is shown in Figure 2. Of the 16 stages available, seven stages were dedicated to extraction and nine stages to scrubbing. Eight stages were used for stripping. After the test was performed, the flowsheet was re-calculated with the flow rates and nitric acid concentrations that were actually measured.

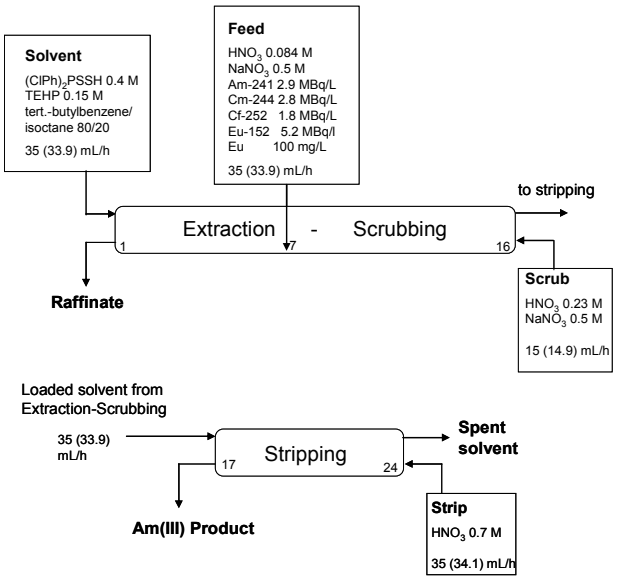

Fig. 2. Flowsheet for the LUCA process with proposed and actually measured (in brackets) flow rates.

The continuous LUCA test was carried out using Chinese 1 cm miniature centrifugal extractors in a counter-current mode. Details of the contactor setup can be found elsewhere [17]. Since only 16 stages were available, stripping was performed on the second day. The solvent loaded with Am(III) (coming from stage 16) was collected in two batches for this purpose and the steady-state fraction was used for stripping.

Main results of the LUCA test

The first objective of the LUCA test was to separate Am(III) from Cm(III) owing to the relatively large Am(III)/Cm(III) separation factor of 6–10. The feed used for this test was an acidic feed containing trace amounts of the trivalent actinides Am(III), Cm(III) and Cf(III) (c.f. Table 1). Europium was also added as a representative for the lanthanides in order to obtain information as to whether this process is also suitable for the selective extraction of Am(III) from a SANEX-type solution, leaving Cm (possibly also Cf) in the lanthanide fraction. No hydrodynamic problems occurred during the test and the material balance was satisfactory. The process decontamination factors $DF_{Am/M(III)}$ and $DF_{feed/raff}$ were calcu-

lated according to the following Eq. 1 and 2, where Q is the flow rate in mL/h and C is the concentration of the element in MBq/L:

TABLE 1.
Composition of the synthetic An(III)/Ln(III) feed used for the single-centrifuge tests and the full counter-current test.

Solute	Concentration
^{241}Am	2.89 MBq/L
^{244}Cm	2.79 MBq/L
^{252}Cf	1.75 MBq/L
^{152}Eu	5.20 MBq/L
HNO_3	0.13 or 0.084 mol/L
$NaNO_3$	0.5 mol/L
Eu	100 mg/L

$$DF_{Am/M(III)} = \frac{Q_{feed} \cdot C_{M(III)\ feed} \cdot C_{Am\ organic\ product\ (stage16)}}{Q_{organic\ phase} \cdot C_{Am\ feed} \cdot C_{M(III)\ organic\ product\ (stage16)}} \quad (1)$$

$$DF_{feed/raff} = \frac{Q_{feed} \cdot C_{feed}}{Q_{raff} \cdot C_{raff}} \quad (2)$$

A high decontamination factor of over 1000 was obtained for americium between the feed and raffinate. As expected, only Am(III) was quantitatively extracted and around 99.8 % Am(III) was back-extracted using 0.7 mol/L HNO_3. A small amount of 0.09 % Am(III) remained in the spent solvent.

The raffinate contained the complete Cm(III) (> 99.5 %), Cf(III) (> 99.9 %) and Eu(III) (>99.9 %) inventory and the contamination of Am(III) (< 0.08 %) was low. On the other hand, the Am(III) product after back-extraction was contaminated with only 0.47 % Cm(III), which resulted in a high $DF_{Am/Cm}$ of 214. A higher decontamination factor of 1744 was measured between Am(III) and Cf(III). As expected from the high Am/Eu separation factors obtained during the batch extraction tests, very good decontamination ($DF_{Am/Eu}$ = 7693) was achieved between Am(III) and Eu(III).

The organic and aqueous steady-state Am(III) and Cm(III) concentration profiles (see Figure 3) and effluent concentrations (Table 2) calculated with the actual flow rates and nitric acid concentrations are in good agreement with the experimental results. In the extraction section, the calculations describe the experiment very well. Only the Am(III) raffinate concentration was slightly overestimated by the calculation (0.17 % calculated vs. 0.077 % measured). The Cm(III) profile in the scrubbing section is described well for stages 8–13 but slightly underestimated for stages 14–16. The experimental concentration profiles of californium are shown also in Figure 3. As expected, the behaviour of Cf(III) is similar to that of Cm(III). Cf(III) is not extracted and the scrubbing efficiently reduces the co-extraction. Only 0.045 % of the initial amount was found in the Am(III) product fraction (Table 2).

The extraction of Eu(III) is very low and scrubbing with 0.23 mol/L HNO_3 decreased the concentration of Eu(III) after just 4 stages to below the detection limit .The behaviour of the other lanthanides was not studied within this test run. From our batch extraction data [11], we assume a similar behaviour for Pr, Nd, Sm and Gd. The lighter lanthanides La and Ce, however, have considerably higher distribution data, although the Am/La and Am/Ce separation factors are still high (i.e. > 40, much higher than the Am/Cm separation factor). Here we expect that more than 4 scrubbing stages are necessary for efficient decontamination.

TABLE 2.
Main results of the LUCA process

Element	% in raffinate (1 aq)	% in product (17 aq)	% in solvent (24 org)	DF feed/raff	DF Am/M
^{152}Eu (γ)	106.7	d.l.	d.l.	0.9	7693
^{241}Am (γ)	0.077	103.3	0.089	1306	–
^{241}Am (α)	d.l.	98.9	d.l.	> 1000	–
^{244}Cm (α)	108.8	0.469	d.l.	0.92	214
^{252}Cf (α)	112.0	0.057	d.l.	0.89	1744
Am calc'd	*0.17*	*99.8*	*0.03*	*573*	–
Cm calc'd	*98.7*	*1.3*	*0.0004*	–	*77*

d.l. = below detection limit

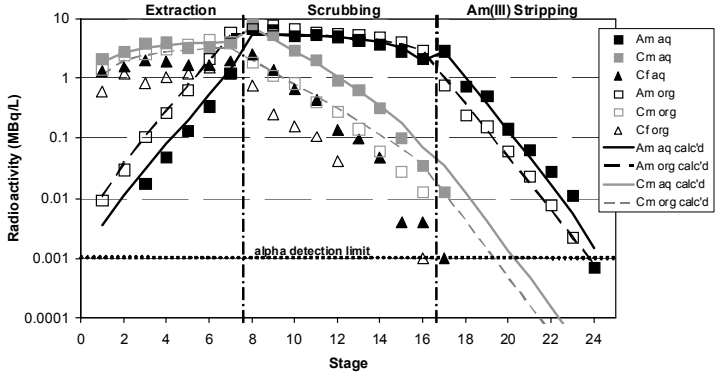

Fig. 3. Experimental (alpha measurements) and calculated steady-state concentration profiles from the counter-current test.

Conclusions

In this paper we showed that the difficult recovery of Am(III) is possible from an acidic solution containing a mixture of trivalent actinides (Am(III), Cm(III) and Cf(III)) and Eu(III) as a lanthanide representative. The LUCA process can be used after a co-extraction process

(e.g. after DIAMEX) for the selective extraction of Am(III), leaving Cm(III) together with the lanthanides in the raffinate fraction. Alternatively, the process can also be run after a SANEX process (e.g. BTBP) for mutual Am/Cm separation.

Acknowledgments
Financial support for this research was provided by the European Commission (project ACSEPT – No. 211267).

References

1. Nash, K. L., Madic, Ch., Mathur, J. N., Lacquement, J.: Chapter 12, *Actinide separation science and technology*. In: The Chemistry of the Actinide and Transactinide Elements, 3rd ed. (Morss, L.R., Edelstein, N.M., Fuger, J., Katz, J.J., Eds.). Springer (2006).
2. Geist, A., Hill, C., Modolo, G., Foreman, M.R.St.J., Weigl, M., Gompper, K., Hudson, M.J., Madic, C.: *6,6`-Bis(5,5,8,8-tetramethyl-5,6,7,8-tetrahydro-benzo[1,2,4]triazin-3-yl) [2,2`]bipyridine, an effective extracting agent for the separation of americium(III) and curium(III) from the lanthanides.* Solvent Extr. Ion Exch. 24, 463–483 (2006).
3. Modolo, G., Odoj, R.: *Synergistic selective extraction of actinides(III) over lanthanides(III) from nitric acid using new aromatic dithiophosphinic acids and neutral organophosphorus compounds.* Solvent Extr. Ion Exch. **17**, 33–53 (1999).
4. Magnusson, D., Christiansen, B., Glatz, J.-P., Malmbeck, R., Modolo, G., Serrano-Purroy, D., Sorel, C.: *Demonstration of minor actinide separation from a genuine PUREX raffinate by TODGA/TBP and SANEX reprocessing.* Internat. Conf. ATALANTE 2008, May 19–23, Montpellier, France (2008).
5. Pillon, S., Somers, J., Grandjean, S., Lacquement, J.: *Aspects of fabrication of curium-based fuels and targets.* J. Nucl. Mater. 320, 36–43 (2003).
6. Mason, G. W., Bollmeier, A.F., Peppard, D.F.: *Partition of oxidized americium from actinides(III) and lanthanides(III).* J. Inorg. Nucl. Chem. **32**, 1011–1022 (1970).
7. Myasoedov, B.F.: *New methods of transplutonium element separation and determination.* J. Alloys Compounds **231/214**, 290–299 (1994).
8. Donnet, L., Adnet, J.M., Faure, N., Bros, P., Brossard, Ph., Josso, F.: *Development of the SESAME process.* 5th Information Exchange Meeting on Actinide and Fission Product Partitioning and Transmutation, Mol, Belgium 1998. OECD-NEA, Paris, France, pp. 161–168 (1999).
9. Baron, P., Lecomte, M., Boullis, B., Simon, N., Warin, D.: *Separation of the long lived radionuclides: current status and future R&D program in France.* Proc. Internat. Conf. GLOBAL 2003 (Atoms for Prosperity: Updating Eisenhower's Global Vision for Nuclear Energy), , November 16–20, New Orleans, U.S.A., pp. 508–511 (2003).
10. Myasoedov, B.F., Maryutina, T.A., Litvina, M.N., Malikov, D.A., Kulyako, Yu.M., Spivakov, B.Ya., Hill, C., Adnet, J.-M., Lecomte, M., Madic, C.: *Americium(III)/curium(III) separation by counter-current chromatography using malonamide extractants*, Radiochim. Acta **93**, 9–15 (2005).
11. Modolo, G., Nabet, S.: *Thermodynamic study on the synergistic mixture of bis(chlorophenyl)dithio-phosphinic acid and tris(2-ethylhexyl)phosphate for separation of actinides(III) from lanthanides(III).* Solvent Extr. Ion Exch. **23**, 359–373 (2005).
12. Modolo, G., Odoj, R.: *Method for separating trivalent americium from trivalent curium.* European patent EP 1664359B1, 03.01.2007.
13. Modolo, G., Kluxen, P., Geist, A., *Demonstration of the LUCA process for the separation of americium(III) from curium(III), californium(III), and lanthanides(III) in acidic solution using a synergistic mixture of bis(chlorophenyl)-dithiophosphinic acid and tris(2-ethylhexyl)-phosphate,* Radiochimica Acta, accepted
14. Geist, A., Weigl, M., Gompper, K.: *Minor actinide partitioning by liquid-liquid extraction: using a synergistic mixture of bis(chlorophenyl)dithiophos-phinic acid and TOPO in a hollow fiber module for americium(III)-lanthanides(III) separation.* Sep. Sci. Technol. **37**, 3369–3390 (2002).
15. Geist, A., Gompper, K.: *Miniature DIAMEX processes in a hollow fibre module micro-plant: process development and optimisation.* Radiochim. Acta **96**, 211–218 (2008).
16. Weigl, M., Geist, A., Gompper, K.: *Kinetics of Am(III)/Cm(III)/Eu(III) extraction with a mixture of di(chlorophenyl)dithiophosphinic acid and TOPO.* Proc. Internat. Conf. GLOBAL 2003 (Atoms for Prosperity: Updating Eisenhower's Global Vision for Nuclear Energy), November 16–20, New Orleans, U.S.A., pp. 1936–1938 (2003).
17. Modolo, G., Asp, H., Vijgen, H., Malmbeck, R., Magnusson, D., Sorel, C.: *Demonstration of a TODGA-based continuous counter-current extraction process for the partitioning of actinides from a simulated PUREX raffinate, part II: centrifugal contactor runs.* Solvent Extr. Ion Exch. **26**, 62–76 (2008).

The crystallization of ThO_2-CeO_2 system

A.A. Bukaemskiy, G. Modolo

Forschungszentrum Jülich GmbH, Institute for Energy Research,(IEF-6), 52425 Jülich, Germany

Corresponding author: a.bukaemskiy@fz-juelich.de

The suitable materials for the immobilization of Pu and MA are studied in Institute of Energy Research (IEF-6, Safety Research and Reactor Technology). Thorium oxide is considered as one of promising matrix for the fixation of the long-lived actinides as target material for transmutation and as a stable material for the long-term final disposal. In the present paper we studied a "soft" co-precipitation route and the thermal and crystallization behavior of thoria-ceria powders using TG-DSC and XRD. It was shown that the synthesized powders constitute a mixture of pure thoria and ceria and $(ThCe)O_2$ solid solution with ceria content different from the initial. For all powders, a solid solution with face-centered cubic, fluorite-type structures and with homogeneous composition of $(ThCe)O_2$ was formed during heating from 700 to 1100°C.

Objectives

Thoria has been considered as an inert matrix for burning excess plutonium from spent fuels in light water reactors [1, 2], as an inert matrix for final disposal [3].Ceramic materials based on thoria are characterised by high physic-mechanical and chemical properties, such as high strength and fracture toughness, high chemical resistance, structural stability and high melting temperature [4].

The co-precipitation method is sufficiently simple and because it is a dust-free technology, it can be adapted for the work with the radiotoxic materials [5]. However, additional quantitative information is required on the evolution of the crystal structure of thoria-based powder depending on the different parameters, such as actinide amount and calcination temperature. Moreover, also require additional information on the homogeneity of the synthesized powder, and its size characteristics after synthesis and at post-annealing.

In the present work, pure ThO_2, CeO_2 and $(ThCe)O_2$ powders with ceria concentrations 25, 50 and 75 mol. % were synthesized by the co-precipitation method. The powder properties depending on temperature were investigated using thermogravimetry coupled with differential scanning calorimetry (TG-DSC) and X-ray diffraction (XRD). Cerium is considered as a surrogate for the tetravalent actinides [6, 7]. The thermal and crystallization behaviour of the powders, in particular, the formation of the stable oxide solid solution during calcination is studied in detail for the whole range of ceria.

Results

The thermal behaviour of the investigated powders was studied by TG-DSC in air atmosphere and results are published in [8]. It was found that the qualitative behaviour of the DSC and TG curves for the ThO_2 and $(ThCe)O_2$ powders studied is independent of the ceria concentration in the material. The results obtained for a pure thoria powder are shown in Fig. 1 as the representative samples.

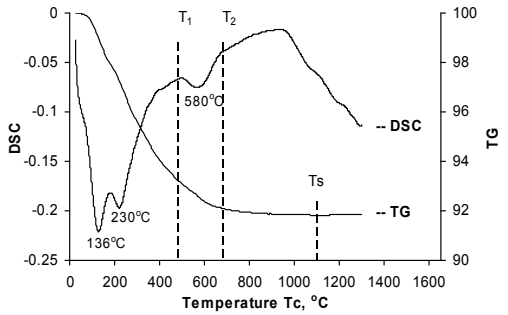

Fig. 1. TG and DSC curves as function of calcination temperatures (Tc).

The ThO_2 powder was characterized by significant mass loss (7.9 %) during heating from 20 to 700 °C (T_2). In this temperature region, mass loss was accompanied by heat consumption, which corresponds to the elimination of adsorbed gases, adsorbed and hydrated water, and impurities. The endothermic effects at 136 and 580 °C correspond to the hydroxide decomposition [9], and endothermic effect at 230 °C – chemical decomposition of ammonia salts [10].

During heating from 700 to 1100 °C, the mass of the sample continued to decrease but the mass loss was negligible (0.24 %). This is associated with the elimination of the residual OH groups from the material [11]. After annealing at temperatures higher than T_S = 1100 °C, the mass remained constant. This temperature T_S appears to be the temperature of stable solid solution formation. For all investigated ThO_2 and $(ThCe)O_2$ powders, the values of temperature T_1, T_2, T_S are presented in [8]. Based on these TG-DSC results, the powders were first calcined in

a DSC furnace at different *Tc* in temperature region from 110 to 1600 °C and then analyzed by XRD (Fig. 2). After drying, all powders crystallized in a face-centered cubic (fcc), fluorite-type structure; however, the degree of crystallinity strongly depends on the annealing temperature (Tc). In order to study material crystallization, a detailed analysis was conducted an X-ray diffraction patterns of the investigated powders after synthesis and after calcination. For all powders, the X-ray diffraction patterns in the range of 2θ from 20 to 85 º were fitted as a sum of Gaussian functions corresponding to each Bragg reflection.

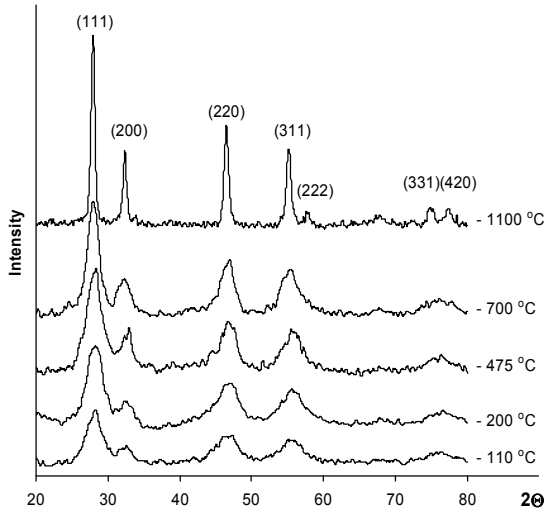

Fig. 2. X-ray diffraction patterns of $(Th_{0.5}Ce_{0.5})O_2$ powders calcined at different temperatures.

The Bragg reflections of ThO_2 powder after drying are sufficiently wide (B ~ 6 º) (Fig. 3 a). The mean nanocrystallite size estimated using the Scherer formula equals 1.8 nm. At a calcination temperature lower than T_2 (700 °C), each Bragg reflection can be approximated by one Gaussian function, as shown in Fig. 3 a for the representative case *Tc* equals 490 °C. At a calcination temperature from T_2 (700 °C) to *Ts* (1100 °C), each Bragg reflection has a complex shape with a wide base and narrow height, and can be approximated by the sum of two Gaussian functions. The representative cases for Tc 850 and 1100 °C are shown in Figs. 3 b, c.

These two Gaussian peaks occur at the same position and differ in terms values of the peak width. The wide first Gaussian peak (denoted as ThO_2* in Figs. 3 b, c) corresponds to the weakly crystallized material where the mean crystallite size increases from 1.8 nm (110 °C) to 6.2 nm (Ts). The crystalline material (second Gaussian peak denoted as ThO_2 in Figs. 3 b, c) is characterized by the value L = 20 nm at temperatures between T_2 and *Ts* and later increases up to 33 nm at temperature *Tc* = 1600 °C. With an increasing calcination temperature, the intensity of the first Gaussian peak decreases, while the intensity of the second Gaussian peak increases. After calcination of the powder at a temperature higher than *Ts*, each Bragg reflection can be approximated by one Gaussian function.

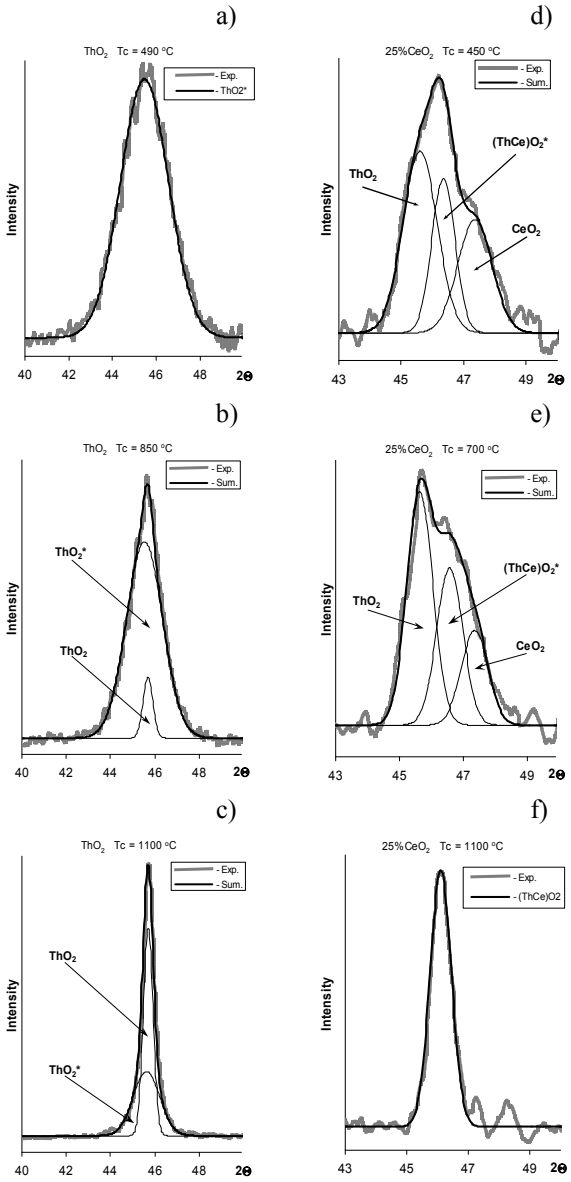

Fig. 3. Fragments of X-ray diffraction patterns of (a, b, c) ThO_2 and (d, e, f) $(Th_{0.75}Ce_{0.25})O_2$ powders calcined at different temperature

Thus, we can assume that the evolution of the Bragg reflection shape at calcination reflects the process of material crystallization, which begins at temperature T_2. The amount of well crystalline material increases with increasing of the calcined temperature and the crystallization mainly finishes at temperature *Ts*.

In the case of pure ceria, the separation of the material on the two components with a different degree of crystallinity was not found. At all calcination temperatures, each Bragg reflection can be approximated by one Gaussian function. The width of the Bragg reflections decreased continuously with an increasing of the calcination tem-

perature. The mean crystallite size increased monotonically from 4.9 nm (Tc = 110 °C) to 56 nm (Tc = 1600 °C).The lattice parameters of pure ThO_2 and CeO_2 were determined from all XRD reflections in the range of 2θ from 20 to 85 º at the different temperatures. The results for thoria (solid, black quadrates and solid line) and ceria (solid, black rhombus and solid line) are shown in Fig. 4.

As shown in Fig. 4, the lattice parameters decreased smoothly with increasing Tc, and at the calcination temperature 1100 °C and higher, the values of a correlate with the reference dates for the well-calcined oxides, for ThO_2 – a = 5.594 Å (a = 5.597 Å [12]) and for CeO_2 – a = 5.410 Å (a = 5.411 Å [13]). The $(ThCe)O_2$ powders crystallized directly after drying in a face-centred cubic, fluorite-type structure (Fig. 2). For the calcination temperature from 110 to 700 °C, each Bragg reflection had a complex shape and can be approximated well by the sum of three Gaussian functions, as shown in Figs. 3 d, e for the representative system $(Th_{0.75}Ce_{0.25})O_2$.

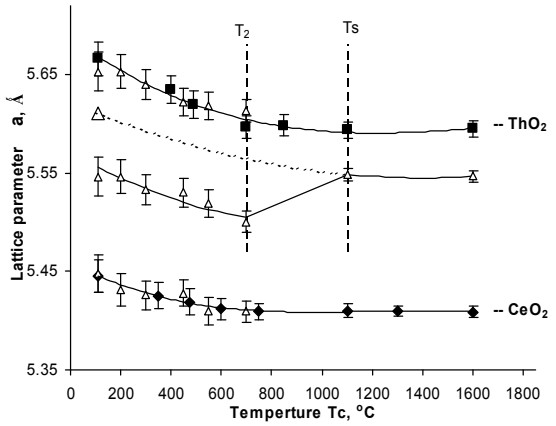

Fig. 4. Lattice parameter as functions of calcination temperature for the ThO_2, CeO_2 and $(Th_{0.75}Ce_{0.25})O_2$ powders.

These three Gaussian functions differed in the intensity, position and width of the peak. At fixed Tc, with increasing ceria content, the intensity of the first Gaussian peak decreased, while the intensity of the third Gaussian peak increased. Moreover, the positions of the first, second and third Gaussian peaks remained almost constant at the different ceria contents. For all powders calcined at different Tc, the lattice parameters were calculated for all three series of Gaussian peaks. The results are shown in Fig. 4 as empty triangles.

For all $(ThCe)O_2$ powders, at temperatures from 110 °C to T_2, the values of the lattice parameters for the series of first Gaussian peaks agreed over the range of experimental accuracy with those of the lattice parameters for pure thoria. The values of the lattice parameters for the series of third Gaussian peaks agreed with the values of the lattice parameters for pure ceria. The lattice parameters also decreased continuously with increasing calcination temperatures. In turn, the series of second Gaussian peaks corresponds to the solid solution (denoted as $(ThCe)O_2$* in Figs. 3 d, e) with a ceria content different from the initial one. At fixed temperatures, the values of the lattice parameters for all three powders over the range of experimental accuracy are equal, i.e. the composition of the solid solution formed is independent of the initial ceria content. As is the case for pure oxides, the lattice parameters also decreased continuously with increasing Tc in the temperature region from 110 °C to T_2. Moreover, the dependencies of lattice parameter (a) on the temperature Tc for the $(ThCe)O_2$* can be described as a single dependence for all investigated powders.

Thus, we can assert that after synthesis and drying and up to 700 °C (T_2), the investigated powders are a mixture of pure thoria, ceria oxides and solid solution $(ThCe)O_2$* with a ceria content different from the initial one. Moreover, the composition of the solid solution formed is independent of the initial ceria content. After calcination of the powders at temperature 1100 °C (Ts) and higher, each Bragg reflection became narrow and was successfully approximated by one Gaussian function, as shown in Fig. 3 f for the representative system $(Th_{0.75}Ce_{0.25})O_2$. For the $(ThCe)O_2$* solid solution, the unusual behavior of $a = a(Tc)$ dependencies occurred in the temperature region from 700 °C (T_2) to 1600 °C, which was caused by the material crystallization and the formation of the solid solution with the initial ceria-thoria content.

For the $(Th_{0.75}Ce_{0.25})O_2$ powder, the lattice parameters increased greatly from 5.505 to 5.549 Å with increasing Tc from 700 to 1100 °C (Ts). At the next calcination, they decreased slightly to 5.546 Å (Fig. 4). For the $(Th_{0.5}Ce_{0.5})O_2$ powder, at temperatures higher then T_2, the lattice parameters remained constant. For the $(Th_{0.25}Ce_{0.75})O_2$ powder, the lattice parameters decreased greatly from 5.505 to 5.464 Å with increasing Tc from T_2 to Ts. At the next calcination, they decreased slightly to 5.458 Å.

Thus, the given above facts are evidence that after calcination at Tc = 1100 °C, all investigated powders form homogeneous $(ThCe)O_2$ solid solutions with a ceria content equal to the initial one. The formation of the homogeneous $(ThCe)O_2$ solid solutions from the mixture of pure thoria, ceria oxides and $(ThCe)O_2$ solid solution with a ceria content different from the initial one occurs in the temperature range from 700 to 1100 °C.

The lattice parameters calculated from XRD patterns for all investigated powders after calcination at 1100 and 1600 °C are plotted as a function of the ceria content in Fig. 5. The experimental data are described by a linear dependence (Vegard's rule) and they correlate with the results presented in [14]:

$$a, Å = -1.84 \cdot 10^{-3} \cdot C_{Ce} + 5.594 \quad (1)$$

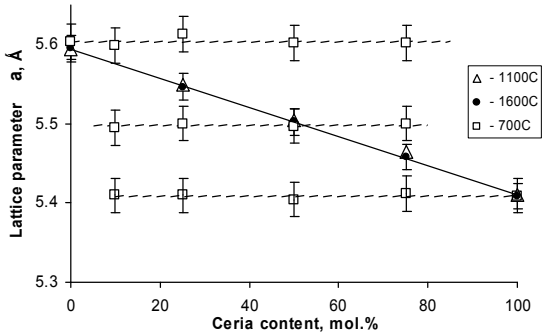

Fig. 5. Lattice parameter as functions of the ceria content.

For $(Th_{0.75}Ce_{0.25})O_2$, $(Th_{0.5}Ce_{0.5})O_2$ and $(Th_{0.25}Ce_{0.75})O_2$ powders after drying, the possible values of lattice parameters in the case of the thoria-ceria content equal initial composition can be estimated from the values of *a* for pure thoria and ceria after drying (5.666 and 5.445 Å, correspondently) and from the assumption that lattice parameters for the $(ThCe)O_2$ solid solution after drying obey also the Vegard's rule:

$$a, \text{Å} = -2.21 \cdot 10^{-3} \cdot C_{Ce} + 5.666$$

These values are equal to 5.611, 5.556 and 5.501 Å for the powders with 25, 50 and 75 mol.% ceria content, respectively. These values and their assumed lattice parameter dependencies on temperature are plotted in Fig. 4 as an augmented empty sign and the dotted lines. As shown, in the temperature range from 110 to 700 °C, the experimental *a = a(Tc)* dependency is situated lower than the calculated curves for $(Th_{0.75}Ce_{0.25})O_2$ and for $(Th_{0.5}Ce_{0.5})O_2$ powders, while it is higher for $(Th_{0.25}Ce_{0.75})O_2$ powder.

The values of the lattice parameters for the powders after calcination at 700 °C are presented in Fig. 5. The results shown clearly demonstrate that the powders investigated are a mixture of pure ThO_2, CeO_2 and $(ThCe)O_2$* solid solution with a ceria content different from the initial one. The lattice parameter of this solid solution is independent of the initial ceria content and equal to 5.499 Å (broken horizontal lines), which corresponds to the value of ceria content equal to 55.2 mol.% as estimated by equation (1).

Summary

$(ThCe)O_2$ powders were obtained by a co-precipitation method and studied in detail using TG-DSC and XRD. It was shown that the synthesized powders contained a mixture of pure thoria, ceria oxides and $(ThCe)O_2$ solid solution with ceria contents different from the initial. The composition of the formed solid solution is independent of the initial ceria content and amounts to 55.2 mol.% ceria. The formation of the homogeneous $(ThCe)O_2$ solid solutions from this mixture occurs in the temperature region from 700 to 1100 °C. After calcination at Tc = 1100 °C, all powders investigated formed homogeneous $(ThCe)O_2$ solid solutions with a ceria content equal to the initial one. All powders were characterized by face-centred cubic, fluorite-type structures, without any apparent segregation of ceria or thoria. The $(ThCe)O_2$ lattice parameter was found to be a function of ceria content according to Vegard's rule.

References

1. H. Akie, T. Muromura, H. Takano, S. Matsura, Nucl. Technol. 107 (1994) 182-192.
2. C. Lombardi, L. Luzzi, E. Padovani, F. Vettraino, Prog. Nucl. Energ. 38 (2001) 395-398.
3. S. Hubert, K. Barthelet, B. Fourest, G. Lagarde, N. Dacheux, N. Baglan, J. Nucl. Mater. 297 (2001) 206-213.
4. J. Belle, R.M. Berman, *Thorium dioxide: Properties and Nuclear applications,* Government Printing office, Washington, D.C., 1984.
5. C. Degueldre, J.M. Paratte, J. Nucl. Mater. 274 (1999) 1-6.
6. H. Matzke, V.V. Rondinella, T. Wiss, J. Nucl. Mater. 274 (1999) 47-53.
7. W.L. Gong, W. Lutze, R.C. Ewing, J. Nucl. Mater. 227 (2000) 239-249.
8. D. Barrier, A.A. Bukaemskiy, G. Modolo, J. Nucl. Mater. 352 (2006) 357-364.
9. D.R. Moorehead, E.R. McCartney, J. Aust. Cer. Soc. 12 (1976) 27-33.
10. Brusset, I., Leveau, F., Spinat, P., Trani, A., Verollet, J., *Le nitrate d'ammonium, Description, production, utilisations et précautions d'usage,* Institut National Polytechnique de Toulouse, 2002
11. A. Aronne, A. Marotta, P. Pernice, M. Catauro, Therm. Acta 275 (1996) 75-82.
12. JCPDS, International Centre for Diffraction Data, 42-1462.
13. JCPDS, International Centre for Diffraction Data, 43-1002, 34-0394.
14. A.K. Tyagi, B.R. Ambekar, M.D. Mathews, J. All. Comp. 337 (2002) 277-281.

Layered double hydroxide containing Zr-IV

H. Curtius[1], K. Ufer[2], K. Dardenne[3]

[1]*Forschungszentrum Jülich GmbH, Institute for Energy Research, (IEF-6),D-52425 Jülich, Germany*
[2]*Institut für Mineralogie, TU Bergakademie Freiberg, Germany*
[3]*Institut für Nukleare Entsorgung (INE), Forschungszentrum Karlsruhe, Germany*
Corresponding author: h.curtius@fz-juelich.de

In order to contribute to the long-term safety analysis of direct disposed research reactor fuel elements, the corrosion behavior of these fuel-types in final repository relevant salt brines was determined. Due to the corrosion processes, radionuclides were mobilized first, but then trapped by the formed secondary phases. A Mg-Al layered double hydroxide (LDH) with chloride as interlayer anion was identified as one crystalline secondary phase component. The possibility to incorporate zirconium-IV into the lattice structure of the Mg-Al-Cl LDH was investigated by a co-precipitation process. The element zirconium was chosen because it has a low adsorption cross section for neutrons, and is therefore used for nuclear energy applications, such as for cladding fuel elements. The synthesized material was analyzed by powder X-ray diffraction (XRD) combined with a Rietveld refinement. Due to a recursive calculation inside the Rietveld refinement, it was possible to derive structural parameters of the disordered LDH. Further on, the Mg-Al-Zr-LDH was analyzed by EXAFS and the results did show that Zr is the central metal atom coordinated by 5 OH groups and by one chloride.

Introduction

In Germany, the direct disposal of spent fuel elements is under investigation. At IEF-6 the work is focused on research reactor fuel element. Two different fuel-types are under investigation. The dispersed metallic UAl_x-type and the U_3Si_2-Al-type.At present three research reactors, the FRM-II-reactor (München), the FRG-I-reactor (Geesthacht) and the BER-II-reactor (Berlin) with a thermal output higher than 5 MW are in operation in Germany. In these reactors dispersed U_3Si_2-Al-fuel is used. In general, three possible back-end options for irradiated research reactor fuel elements exist in Germany [1]: first, irradiated research reactor fuel elements of USA origin can be sent back when these fuels were taken out of the reactor not later than May 2006. This affects basically the dispersed metallic UAl_x-Al-fuel, which was used in the FRJ-II-reactor (Jülich) till May 2006. Secondly, reprocessing in Great Britain or France is possible and it will be performed with respect to economical reasons. Thirdly, dry interim storage and later on, direct disposal in deep geological formations has been taken into account too. A possible repository under consideration is a salt mine, and the accident scenario for long-term safety analysis is water ingress. Different leaching experiments with the dispersed metallic UAl_x-Al-fuel (fuel used in the material test reactor FRJ-II) [1] in highly-concentrated salt brines at 90 °C showed that the radionuclides were rapidly mobilized, but then trapped by the corrosion products [2]. Investigations [3] of these secondary corrosion products as a barrier against radionuclide migration indicated that one component is a Mg-Al-Cl LDH, also referred as a hydrotalcite-like compound (HTlc).

LDHs may be described by the general formula:
$[M(II)_{1-x} M(III)_x (OH)_2]^{x+} (A^{n-})_{x/n} \; m\, H_2O$, where M(II) and M(III) are di- and trivalent metals respectively, and A^{n-} is an anion. Their structure is based on brucite-like layers, in which a divalent cation is located in the centre of oxygen octahedra and two-dimensional infinite layers are formed by edge-sharing of the octahedra. Partial isomorphous substitution of divalent cations for trivalent ones results in a positive charge on the layers. This charge is compensated by the presence of anions in the interlayer [4]. In the free space of this interlayer, water molecules are also present. The main features of LDH structures and of LDH properties are determined by the nature of the brucite-like sheet, by the type of stacking of the brucite-like sheets, by the amount of water and by the position and type of anions in the interlayer. It should be pointed out that a change in the brucite-like layer will result in different properties of the LDH. A change in the brucite-like sheet is possible by changing the stoichiometry of the metal ions present or by an exchange of the metal ions.

Objectives

We already demonstrated that an isomorphous substitution of the trivalent aluminium, present in the Mg-Al-Cl LDH, by the trivalent europium [5], and by the trivalent samarium [6], is possible. Within this substitution the net positive charge in the brucite layer remains constant, hence the value of the AEC (anion exchange capacity) remains constant too. An increase of the AEC value can be achieved by increasing the number of trivalent ions in the layer within permissible limits. Alternatively, partial substitution of the Mg-II or Al-III ion by a tetravalent metal ion, may increase the net positive charge in the

[1] The UAl_x-Al fuel contains of the FRJ-II reactor contains 20 wt% U-Al alloy with an initial enrichment of 80 % in ^{235}U. The fuel alloy plates with a thickness of 0.6 mm (meat) are covered on both sides with aluminium claddings of 0.38 mm.

brucite layer and hence the AEC value, too. An increase in the AEC value is desirable because then the LDH can remove higher amounts of anionic radionuclide species. The influence of the increased AEC-value in view of the retardation of anionic species was already studied by Das et al. [7]. The first synthesis of a Mg-Al-LDH containing Zr in the brucite layer but with carbonate as interlayer anion was reported by Velu et al. [8]. Nevertheless, these results were discussed by Intissar et al. [9] in detail. By use of X-ray absorption and Mössbauer spectroscopy they showed, that the tetravalent cation is segregated from the LDH structure and forms amorphous M-IV oxide-like particles.
In the present paper we report the preparation and detailed characterization of a layered material possessing the hydrotalcite-like structure containing magnesium, aluminium and the tetravalent element zirconium in the hydroxide layer with chloride as interlayer anion. From XRD and EXAFS measurements the presence of Zr IV oxide particles can be ruled out. Nevertheless due to the bigger ionic radius of Zr-IV (0.74 Å) compared to the ionic radius of Al-III (0.51 Å) a defect in the lattice structure can not be excluded.

Experiments
Deionised water was boiled and stored under an argon atmosphere before use. The chemicals were of analytical grade and used without further treatment. All experiments were performed under an argon atmosphere.

Synthesis of the Mg-Al-Zr-Cl LDH
The Mg-Al-Zr-Cl LDH was obtained according to the following co precipitation process: 250 mL of water were placed in a three-necked glass flask and a pH of 10 was adjusted using 2 M NaOH. A mixed aqueous solution of MgCl2·6H2O (0.3M) and AlCl3·6H2O (0.09M) and ZrOCl2·8H2O (0.01M) in 250 mL water was added over a period of five hours while the pH was maintained at 10 by addition of 2 M NaOH. The temperature was maintained at 70 °C. After the addition was complete, the temperature was raised to 90 °C and stirring was continued for 24 hours. After cooling to room temperature, the formed precipitate was filtered and then dialyzed at 60 °C. For that purpose a dialysis hose was filled with the substance and placed in 2 l vessel containing deionised water. The water was changed until it was chloride-free (chloride measurements were performed with the cuvette test LCK 311, DR. LANGE). The precipitate was filtered and dried in a desiccator.

Chemical analysis
The obtained substance was characterized by photometry, DTA-TGA, FTIR, ICP-OES, SEM-EDX, EXAFS and XRD. For DTA-TGA, SEM-EDX, XRD, EXAFS and FTIR measurements, dry samples were milled to powder. For photometric and ICP-OES measurements the solid samples were dissolved in 2 M HNO_3. Furthermore one g of the synthesized Mg-Al-Zr-Cl LDH was treated with 50 mL of an ammonium carbonate solution (one mol/L) at room temperature for 24 hours. This procedure was performed to distinguish between sorbed and incorporated Zr species. A change in the metal ion stoichiometry is expected, when Zr is only sorbed and not incorporated. Then the solid was separated by filtration, washed with 10 mL water and dried at 70 °C.
500 µL of the filtrate was added to 49.5 mL of a 0.1 M nitric acid solution and this solution was analyzed by ICP-OES in order to determine the amounts of Mg, Al and Zr. To determine the Mg, Al and Zr molar ratios of the solid, an ICP-OES analysis was performed as follows:
100 mg of the solid was dissolved in 10 mL 2 M nitric acid. This solution was diluted (1 to 1000) with a 0.1 M nitric acid solution and the measurement was performed.
To obtain detailed information about the incorporation of Zr, investigations with XRD and EXAFS were performed.

X-ray diffraction (XRD)
Prior to the X-ray diffraction measurements, an internal standard (10.0 wt.-% zincite) was added and the sample was hand-ground in an agate mortar. For the specimen preparation the top loading technique was used. The sample was measured on a 3003TT (General Electric) diffractometer (Bragg-Brentano geometry, Cu-K_α radiation generated at 40 kV and 40 mA) equipped with an automatic divergence slit irradiating 10 mm sample length, a 0.5 mm detector slit, a secondary beam graphite monochromator, a point detector and a sample spinner. The sample was measured from 5° to 85° 2Θ with a step size of 0.03° 2Θ and a measuring time of 20 sec per step.

Rietveld refinement
The principle of the Rietfeld method [10] consists of the computation of synthetic diffraction patterns from a given structural model. This data will be fitted to experimental data by a non-linear least squares minimization. The quality of the refinement can be judged by the agreement index R_{wp}, which contains the differences of measured and observed data and its comparison to R_{exp}, the theoretical minimum value for R_{wp} [11].
The Rietfeld analysis allows an insight in structural details of crystalline materials and therefore it is suitable for the characterisation of the LDH.
For the refinement, the program BGMN was used [12].
BGMN contains a structure description language and offers the possibility of a complex manipulation of the structure factors and a solver for linear equation systems. Therefore a recursive treatment of diffraction effects from faulted layer stackings, similar to DIFFaX simulations [13] can be performed within a Rietveld refinement [6].

From previous investigations [5] it is known that LDHs develop a disordered stacking of the two polytypes $2H_1$ and $3R_1$. Both polytypes form trigonal prismatic interlayer polyhedra. In the $3R_1$ structure adjacent layers are translated by a stacking vector (2/3,1/3,1/3) relative to

each other. The $2H_1$ polytype is formed by an alternate stacking of layers which are rotated around 180° parallel to the adjacent layers. In this work the probability of these two stackings could be refined. The layer structure is derived from a description of a Cl-LDH ($3R_1$) by Ennadi et al. [14] Due to the disordered stacking, the symmetry is reduced from the original point group R-32/m (3 layers per unit cell) to P3m1 (one layer per unit cell). In addition to the atomic positions of the interlayer atoms (Cl and oxygen to represent water) as proposed by Ennadi et al. [14], several further positions were tested. The initial occupancies of atomic positions are derived from chemical analysis. The occupancies of the cations were not refined. For ZnO only lattice parameters, peak broadening parameters and a scaling factor was refined. As non-structural parameters, the zero point, the sample displacement error and a Lagrange polynomial of 5th degree for background modeling were refined. BGMN includes a fundamental parameter approach to model the peak profiles [15]. The instrument-dependent part of the diffraction profile is predetermined by a ray tracing procedure.

Extended x-ray absorption fine structure (EXAFS)
Zr K X-ray absorption fine structure (XAFS) spectra are recorded at the INE-beamline (ANKA, Karlsruhe, Germany). Spectra are energy calibrated to the first inflection point in the XANES of a Zr foil (17.998 keV) measured simultaneously. The Zr-doped LDH XAFS is recorded at room temperature in transmission-mode using Ar-filled ionization chambers at ambient pressure. Ge<422> crystals are used in the monochromator, operating in fixed-exit mode. The incident intensity is held constant by means of a piezo-driven feedback system. The parallel alignment of the crystal faces is detuned to ~70% of the maximum beam intensity. The XAFS sample is pressed in dried form into a polyethylene pellet of 13mm diameter.

Table 1: Metric parameters of the LDH with Mg/Al as center (R=distance between the central atom chosen, here Mg/Al (both share the same crystallographic site) and the backscatterer atom, N=coordination numbers) [18]

Backscatterer	N	R (A) LDH
O (from OH)	6	2.03
Al/Mg	6	3.06
O (from OH)	6	3.67
C	2	4.00
O	6	4.19

EXAFS fits are performed with Artemis [16] part of the Ifeffit package [17], using phase and amplitude data calculated for a 9 atom cluster derived from the undoped LDH structure [18] (Table 1). The cell parameters are increased to account for the larger size of the Zr cation. Single path scattering files for phase and amplitude are used for the second coordination sphere. The k-range used for the fit is [2.33-13.93$Å^{-1}$] and fits are performed in the R-space on the k^2-weighted data.

Results
Characteristics of LDHs
The Mg-Al-Zr-Cl LDH was prepared according to a described co-precipitation method [19]. Little modifications were performed with regard to the purification and drying steps. For the synthesized double layered hydroxide a Mg/Al/Zr mole ratio of 3:0.93:0.099 was determined by ICP-OES. Chloride was determined photometrically. In the DTA-TGA thermogram the first endothermic peak occurs between room temperature and 275 °C, with its maximum at 142.5 °C, corresponding to a weight loss of 14.7 %, and is due to desorption of the interlayer water. The second endothermic peak between 275°C and 600 °C indicates partial dehydroxylation in the main layer and elimination of chloride in the interlayer. The IR-spectra show strong hydroxyl and water stretching and bending bands at 3482 cm^{-1} and 1636 cm^{-1}. Metal-O-vibration bands appear in the region 1000 cm^{-1} to 550 cm^{-1}. From these results the formula of the Mg-Al-Zr-Cl LDH was derived as
$[Mg_3Al_{0.93}Zr_{0.099}(OH)_8]Cl_{0.94}(CO_3^{2-})_{0.03} \cdot 2.71H_2O$.

The morphology of the Mg-Al-Zr LDH obtained was investigated by SEM. The sand rose crystal structure (Figure 1), typical for LDHs [20], can be clearly seen.

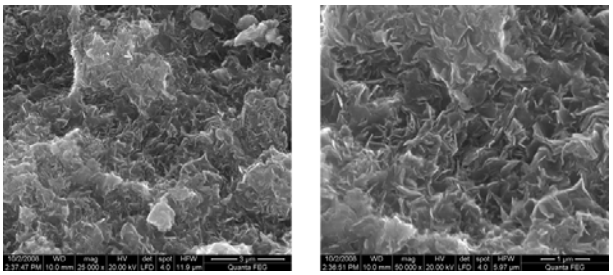

Fig. 1: Morphology of the Mg-Al-Zr-LDH

Then the element distribution was determined by EDX and theses results did show a homogeneous distribution and no other phase was observed.

For the solid a specific surface area of 48 m^2/g was determined by BET and a cationic exchange capacity of 66 mmol/100 g was obtained by a complexation reaction with Cu-II-triethylentetraamin.

Furthermore, the treatment of the Mg-Al-Zr-Cl LDH with an ammonium carbonate solution [21] did not result in any change of the Mg-Al-Zr molar ratios, indicating that the Zr is incorporated. For Zr species, which are sorbed at the LDH surface, we expect an interaction with the strong complexation agent, leading to the formation

of carbonate complexes. These components were neither detected in solution nor in the solid.

XRD measurements

Table 2 shows the structural results of the Rietveld refinement of the Mg-Al-Zr-Cl LDH. It was found that the original position for the interlayer chloride, as proposed by Ennadi et al. [14] did not lead to a satisfying result. Attempts to refine the position in the a1-a2 plane showed that the chloride has a tendency to move on a position perpendicular to the hydrogen, which corresponds to the Wyckoff position b (space group P3m1). In the final refinement only the interlayer water was positioned on the site proposed by Ennadi et al. [14] and chloride was fixed on Wyckoff position b. However, the occupancy of the chloride strongly decreased. This indicates that this position is also not suitable for a satisfying description of the atomic arrangement. This is illustrated in the strong misfit of the intensity of the 110 reflection (angular position at 60.06) (Figure 2).

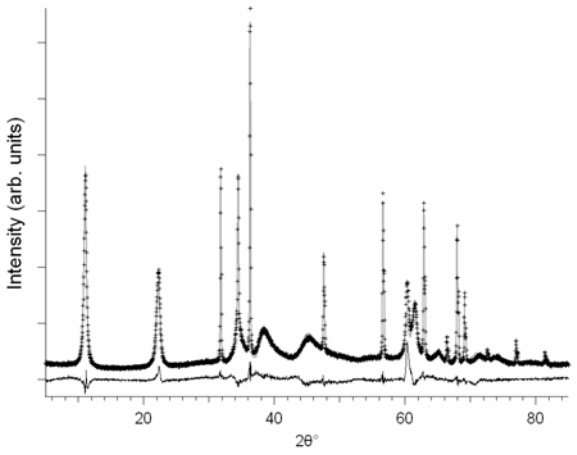

Fig. 2: Rietveld refinement of the Mg-Al-Zr-Cl LDH. Gray line: calculated intensity; +: observed intensity, black line: difference curve.

Unfortunately, so far there exists no suitable model in literature to describe the position of the chloride. Apart from this drawback, the refinement produced some significant structural parameters. The probability for the $3R_1$ stacking is close to 0.5, this shows that this LDH is highly disordered. The a and c lattice constant show typical values for a Cl LDH. Both values, the stacking probability and the lattice constants, have no influence on the intensity of the 110 reflection [5].

The initial content of the ZnO admixture was refined as 10.96 wt.%. This overestimation could be explained by an additional amorphous component (9.7 wt.%, ESD = 1.3 wt.%). However, the uncertainties in the determination of the amorphous content are relatively high and, consequently, a quantification of a small amount with large error seems to be critical.

Table 2: Refinement results of Mg-Al-Zr-Cl-LDH (Rwp and Rexp =agreement indices, a and c=lattice constants, p(3R1)=probability for 3R1 stacking, p(Cl) and p(H2O)= occupancy of Cl resp. H2O, ESD= estimated standard deviation).

	Start parameters	Refinement	ESD
R_{wp} [%]		9.14	
R_{exp} [%]		3.38	
a [Å]	3.06	3.0718	0.0011
c [Å]	8.00	8.0002	0.0045
p(3R1)	0.5	0.5129	0.0044
p(Cl)	0.235	0.0264	0.0051
$p(H_2O)$	0.25	0.0777	0.0012
LDH [wt.%]		89.04	0.14
ZnO [wt.%]		10.96	0.14

EXAFS measurements

The data are well reproduced using 3 shells within the FT range [1.1-3.4Å] as shown Fig.3. The first coordination sphere contains 5 O atoms at 2.13Å with a Debye-Waller factor (σ^2) of 7.0 10^{-3}Å^2 and 1 Cl atom at 2.45Å with a σ^2 of 9.8 10^{-3}Å^2. The Debye-Waller factor is a parameter accounting for the molecular structural and thermal disorder of a sample, static and thermal disorder from the point of view of the absorber atom (here Zr). It traduces the distance distribution of the coordination shell considered. The presence of a Cl atom was not expected in the first coordination shell but no satisfactory fit can be achieved without adding the chlorine atom.

The structural incorporation of the Zr dopant is comparable to Eu in LDH [5]. The Zr is six-fold coordinated but a chlorine atom has replaced an oxygen atom in the first coordination shell. As for Eu-doped LDHs, the Al shell is more distant as expected for isotropic extension of the unit cell. Circa 2 Al atoms are found at 3.51Å [1.7 Al at 3.45Å for Eu]. The reduced Al coordination number compared to the expected value of 6 (see Table 1) as well as the missing associated O shell (from OH), indicates either disorder in the Zr near neighbour structure, with larger radius, or that Zr does not replace Al/Mg exactly at their lattice position. No Zr-Zr interaction can be evidenced, excluding the formation of cluster or polynuclear species such in Zr oxide or hydroxide within the EXAFS detection limit. It is likely that the Zr is located out of the Al/Mg layer, bonding then with two Al/Mg. The Cl atom will then come in the vicinity of Zr and could explain that one Cl integrates the first coordination shell. These results are also compatible with a bidentate sorption species but this possibility of a sorption species is ruled out by the results of the treatment of the Mg-Al-Zr-Cl LDH with an ammonium carbonate solution as reported in this paper. Therefore, we argue as for the Eu case that the Zr

atom is likely incorporated into the LDH structure but as a defect.

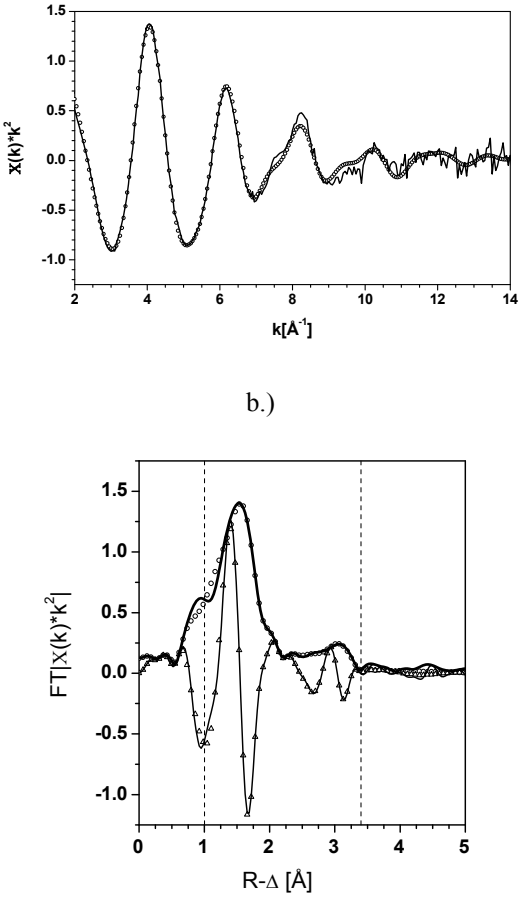

Fig. 3: (a) k2-weighted Zr L3 EXAFS of the sample (solid line) and fit result (open circles); (b) FT magnitude (thick solid line), imaginary part (thin solid line), and fit result (open triangles and circles). FT is performed in the range 2.3-13.9Å-1. FT fit range borders are indicated with dashed lines

Conclusions

Within a couple of months a non-irradiated metallic UAl_x-Al fuel element sample corroded completely in the presence of Fe-II ions in a final repository salt brine solution at 90 °C. In the corrosion products a crystalline phase component was identified as Mg-Al-Cl LDH. The ability of this component to retard radionuclide species by incorporation was investigated. As element species the tetravalent zirconium was chosen.

A synthesis of a Mg-Al-Zr LDH with chloride as interlayer anion was performed. From the analytical data the formula of the Mg-Al-Zr-Cl LDH can be derived as $[Mg_3Al_{0.93}Zr_{0.099}(OH)_8]Cl_{0.94}(CO_3^{2-})_{0.03} \cdot 2.71H_2O$. Proofs for the successful incorporation of the tetravalent Zr can be given as follow:

- The molar ratio of Mg-Al-Zr did not change, when this LDH was treated with an ammonium carbonate solution. No Zr was detected in solution and the remaining solid, analyzed by XRD, showed only the typical LDH reflexes.
- SEM-EDX investigations clearly showed the typical sand rose structure and a homogeneous element distribution. No by products were detected.
- The Rietveld refinement of the XRD measurement showed that the synthesized material consists of a LDH with a high degree of stacking disordering. No additional phases could be detected directly.
- Investigations performed by EXAFS spectrometry did show clearly, that in the first coordination shell of the Zr atom 5 OH groups and one chloride atom is present, hence Zr possess an octahedral.. No Zr-Zr interaction can be evidenced, excluding the formation of cluster or polynuclear species such in Zr oxide or hydroxide within the EXAFS detection limit. Nevertheless, the exact position of the Zr in the crystal lattice structure of the LDH is not clear yet. Because of the high degree of stacking disordering of the LDH, especially improvements of the structural models are necessary. This work is in progress.

Outlook

In order to contribute to the long-term safety analysis of final disposed research reactor fuel elements these results indicate that Zr-IV can be incorporated in the lattice structure of the Mg-Al-LDH. Further on this indicates the wide variations to form different LDH-types and hence the ability to retard radioactive species. In future it is aspired to describe the mechanism of formation and the thermodynamic stability of this LDH-type.

References

[1] Thamm, G.: *Disposal of irradiated fuel elements from German research reactors – Status and Outlook;* Trans. Int. Conf. Research Reactor Fuel Management (RRFM 1999), Bruges, Belgium, 159 (1999).

[2] Brücher, H., Curtius, H., Fachinger, J., Kaiser, G., Mazeina, L., Nau, K.: *Untersuchungen zur Radionuklidfreisetzung und zum Korrosionsverhalten von bestrahltem Kernbrennstoff aus Forschungsreaktoren unter Endlagerbedingungen*, Report Forschungszentrum Jülich, Jül-4104, ISSN 0944-2952 (2002).

[3]. Mazeina, L., Curtius, H., Fachinger, J., Odoj, R.: *Characterisation of secondary products of uranium-aluminium material test reactor fuel element corro-*

sion in repository-relevant brine, J. Nucl. Mater. **323**, 1 (2003).

[4] Miyata, S.: *The synthesis of hydrotalcite-like compounds and their structures and physico-chemical properties,* Clays and Clay Min. **31**, 369 (1975).

[5] Stumpf, T., Curtius, H., Walther, C., Dardenne, K., Ufer, K., Fanghänel, T.: *Incorporation of Eu(III) into hydrotalcite: a TRLFS and EXAFS study*, Env. Sci. Technol. **41 (9)**, 3186 (2007) and Curtius, H.; Ufer, K.: *Eu incorporation behaviour of a Mg-Al-Cl layered double hydroxide*, Clays and Clay Min. **55 (4)**, 354 (2007).

[6] Ufer, K., Kleeberg, R., Bergmann, J., Curtius, H., Dohrmann, R.: *Refining realstructure parameters of disordered layer structures within the Rietveld method.* Zeitschrift für Kristallographie, in press DOI-10.1524/zksu.2008.0020.

[7] Das, N. N., Konar, J., Mohanta, M. K., Srivastava, S. C.: *Adsproption of Cr(VI) and Se(IV) from their aqueous solutions onto Zr 4+- substituted ZnAl/MgAl-layered double hydroxides: effect of Zr 4+ substitution in the layer*, J Colloid Interface Sci. **270**, 1 (2004).

[8] Velu, S., Ramaswamy, V., Ramani, A., Handa, B. M., Sivasanker, S.: *New hydrotalcite-like anionic clays containing Zr4+ in the layers*, Chem. Commun. 2107 (1997).

[9] Intissar, M., Jumas, J-C., Besse, J-P., Leroux, F.: *Reinvestigation of the layered double hydroxide containing tetravalent cations: Unambiguous response provided by XAS and Mössbauer spectroscopy,* Chem. Mater. **15**, 4625 (2003).

[10] Rietfeld, H. M.: *Line profiles of neutron-powder-diffraction peaks for structure refinement*, Acta Cryst. **22**, 151 (1967).

[11] Hill, R.J., Fischer, R.X.: *Profile agreement indices in Rietfeld and pattern-fitting analysis*, J. Appl. Cryst., **23**, 462, (1990).

[12] Bergmann, J., Friedel, P. and Kleeberg, R.: *BGMN – a new fundamental parameter based Rietveld program for laboratory X-ray sources, it's use in quantitative analysis and structure investigations, Commission of Powder Diffraction,.* International Union of Crystallography, CPD Newsletter, **20**, 5 (1998).

[13] Treacy, M.M.J., Newsam, J.M. and Deem, M.W.: *A general recursion method for calculating diffracted intensities from crystals containing planar faults,* Proc. R. Soc. Lond., **A433**, 499 (1991).

[14] Ennadi, A., Legrouri, A., De Roy, A. and Besse, J.P.: *X-ray diffraction pattern simulation for thermally treated [Zn-Al-Cl] layered double hydroxide,* J. Solid State Chem. **152**, 568 (2000).

[15] Cheary, R. W. and Coelho, A. A.: *A fundamental parameters approach to X-ray line-profile fitting*, J. Appl. Crystallography, **25**, 109 (1992).

[16] Newville, M., *IFEFFIT interactive XAFS analysis and FEFF fitting,* J. Synchrotron Rad. **8**, 322 (2001).

[17] Ravel, B., Newville, M.: *ATHENA, ARTEMIS, HEPHAESTUS: data analysis for X-ray absorption spectroscopy using IFEFFIT*, J. Synchrotron Rad. **12**, 537 (2005).

[18] Bellotto, M., Rebours, B., Clause, O., Lynch, J., Bazin, D., Elkaim, E.: *A reexamination of hydrotalcite crystal chemistry,* J. Phys. Chem. **100**, 8527 (1996).

[19] Weiss, A. and Toth, E.: *Untersuchungen zur Synthese, Quellungseigenschaften und Anionenaustausch von kristallchemisch modifizierten Doppelhydroxiden vom Hydrotalkit-Typ*, Jahrestagung der DTTG, Freiberg, 267 (1996).

[20] Mistra, C., Perrota, J.: *Composition and properties of synthetic hydrotalcites,* Clays and Clay Min. **40**, 145 (1992).

[21] Duff, C.M., Coughlin, J.U. and Hunter D.G.: *Uranium co-precipitation with iron oxide minerals,* Geochimica et Cosmochimica Acta, 66, 3533 (2002)

Adsorption of selenium on a Mg-Cd-Al layered double hydroxide

B. Hansen, H. Curtius, R. Odoj

Forschungszentrum Jülich GmbH, Institute for Energy Research, (IEF-6), D-52425 Jülich, Germany
Corresponding author: b.hansen@fz-juelich.de

Leaching experiments with non-irradiated metallic uranium-aluminium research reactor fuel elements in repository-relevant $MgCl_2$-rich salt brine (brine 2), clay pore water (Mont-Terri-type) and granite water (Äspö-type) were performed. As a crystalline secondary phase component so far in brine 2 a Mg-Al LDH with chloride as the interlayer anion was identified. In this work the incorporation of cadmium into the structure of the Mg-Al-Cl LDH was investigated. The synthesis was performed by a co-precipitation method and the Mg-Cd-Al-Cl LDH obtained was characterized. Sorption investigations of selenium on the LDH were performed in water, clay pore water and brine 2. The sorption kinetics was rapid and the equilibrium was reached within a half day. Since the chloride anions in the solutions acted as competing anions for the sorption of selenium, the sorption decreased with increasing amount of chloride anions. The effect of pH on selenium sorption was investigated and a high buffer capacity of the LDH was observed. For the used range of selenium concentration the obtained sorption isotherms were linear. The data were fitted to the Freundlich and Dubinin-Radushkevich equations. The energies of selenium sorption were estimated to be in the range of ion exchange processes.

Introduction

Based on the political decision that there should be no reprocessing of spent research reactor fuel elements (RRFEs) in Germany, the direct disposal in deep geological formations is under consideration. Possible geological formations are granite, clay and salt. In granite and clay formations pore water is always present. In a salt mine water ingress is the accident scenario for long-term safety analysis. In that case highly concentrated salt brines will originate. Hence leaching experiments with non-irradiated metallic uranium-aluminium research reactor fuel elements in repository-relevant solutions were accomplished [1]. The fuel elements corroded completely within one year. The radionuclides were rapidly mobilized but then trapped by the secondary corrosion products. This retardation shows that these secondary phases represent a barrier in the near field against radionuclide migration. Possible retardation processes can be described by adsorption or incorporation mechanisms. In the secondary phases obtained in brine 2 a Mg-Al-Cl LDH was identified as a crystalline component.

The crystal structure of the LDHs consists of brucite-like layers, in which a part of the divalent cations is statistically replaced by trivalent cations [2]. The thereby caused positive charge excess is compensated by interlayer anions. Water is also present in the interlayer. Due to their distinct layered structure and their high anion exchange capacity, LDHs arrested attention in recent years. LDHs are some of the few inorganic anion exchangers that have relatively high capacities of about 3 meq/g [3]. Because of the well-known elemental variability of natural occurring LDHs under repository-relevant conditions different LDH-types can occur.

LDHs can be readily synthesized by coprecipitation methods [4, 5]. The first synthesis of a LDH with Cd instead of Mg with CO_3^{2-} as counter ion was reported by Miyata and Kumura [6], but they obtained a product with small amounts of $CdCO_3$. A pure Cd/Al LDH with NO_3^- and CO_3^{2-} in the interlayer was synthesized successfully by Vichi and Alves [7].

Cadmium is of importance because of its chemical toxicity. Since ^{113}Cd is present in spent RRFEs as fission product (about 10^5 Bq in the used UAl_x-Al fuel sample [1]) it is found in nuclear waste streams. For the immobilization of radionuclides in a repository it is of interest to obtain the information, if a cation with such a big ionic radius in comparison to magnesium (Mg^{2+}: 72 pm, Cd^{2+}: 95 pm, coordination number 6, [8]) can be embedded into the lattice structure of a Mg-Al LDH. Cadmium represents an analogue for radionuclides with big ionic radii, for example radium.

One of the resulting fission products in irradiated research reactor fuel elements is ^{79}Se. Because of its half-life of 6.5×10^4 years and its mobility it is counted among the long term safety-relevant radionuclides for the repository. In this work the experiments were performed with selenite (chemical form of ^{75}Se in the used stock solution: H_2SeO_3 in 0.1 M HCl), because this is the most probable compound of Se appearing under the expected reductive final disposal conditions. The presence of selenate was therefore not expected.

A great deal of the nowadays available literature on the sorption of selenium on LDHs described the sorption only from pure water [9, 10]. You *et al.* [11] and Yang *et al*. [12] studied the sorption of selenium on a Mg-Al LDH, but all experiments were performed in pure water or in aqueous solutions containing the competing

anions only in concentrations of up to 0.025 mol/L and 0.01 mol/L respectively. The sorption of selenite in brine 2, a repository-relevant salt solution, on a Mg-Al LDH and on a Mg-Al-Eu LDH was carried out by Curtius *et al.* [13].

Objectives

In the present work a Mg-Cd-Al LDH was prepared from chloride salts. In this LDH 3.3 % of the molar amount of Mg was replaced by Cd successfully. This Mg-Cd-Al LDH was characterized and the sorption behavior of SeO_3^{2-} in water, clay pore water (Mont-Terri-type) and brine 2 was investigated. Time-dependent analyses and sorption isotherm studies in consideration of the influence of pH were performed.

Experiments

The Mg-Cd-Al-Cl LDH was prepared following the co-precipitation method of Weiss and Toth [14] with minor modifications. First of all 250 mL water was placed in a round flask. A mixed aqueous solution of $MgCl_2 \cdot 6\ H_2O$ (0.29 mol), $CdCl_2 \cdot H_2O$ (0.01 mol) and $AlCl_3 \cdot 6\ H_2O$ (0.1 mol) in 250 mL of water was added over a period of three hours. Meanwhile the pH was maintained at 10 by adding 2 M NaOH drop wise at a temperature of 70°C. Afterwards stirring was continued for 24 h at a temperature of 90°C. The precipitate formed was filtered and then dialyzed at 60°C. After dialysis the solid was filtered again and dried in a desiccator under an argon atmosphere.

For X-ray diffraction (XRD) and differential thermal analysis-thermogravimetric analysis (DTA-TGA) the dry Mg-Cd-Al LDH was milled to powder. Fourier transform infrared spectroscopy (FTIR) was performed using the KBr pellet technique. The amount of Mg, Cd and Al was determined by inductively coupled plasma-optical emission spectroscopy (ICP-OES). The examination of the amount of chloride was accomplished by photometry. To determine the specific surface area by BET the milled solid was sieved up to a particle size less than 0.050 mm. In addition, 1 g of the sample was treated with 30 mL of a 1 M ammonium carbonate solution at room temperature for 24 h. Then the solid was filtered, washed with water and dried at 80°C. An ICP-OES measurement was performed as aforementioned.

The sorption experiments were performed using the batch technique. The samples were stored under an argon atmosphere in glass tubes with occasional shaking. For the sampling procedure the samples were filtered using a 450 nm filter and the pH was measured. The concentration of ^{75}Se in solution was determined by liquid scintillation counting (LSC).

For time-dependent sorption studies 100 µL selenite solution (containing 5.61 x 10^{-15} mol of Se) and 100 mg Mg-Cd-Al LDH was added to 10 mL solution (water, clay pore water or brine 2). The selenite concentration in this mixture was 5.55 x 10^{-13} mol/L. Samples were taken at different time intervals. Blank experiments which were carried out in an analogous manner indicated that the sorption of selenium on the glass walls was negligible.

The desorption behaviour was investigated using the dilution method. First 10 mL solution (water, clay pore water or brine 2) with 100 µL selenite solution and 100 mg LDH was equilibrated. 5 mL of the equilibrated solution was removed in each case and 5 mL new solution (water, clay pore water or brine 2) was added. The analysis of the removed solution was performed as described above. Desorption procedure was repeated five times for each sample.

To obtain the adsorption isotherms to 10 mL solution (water, clay pore water or brine 2) different quantities of the selenite solution and 100 mg Mg-Cd-Al LDH were added. The selenite concentration in the mixtures ranged from 5.33 x 10^{-14} mol/L to 2.67 x 10^{-12} mol/L. After two days the samples were analyzed.

For investigations of the effect of pH on the sorption of selenite 10 mL of the solution (water, clay pore water or brine 2) and 100 µL selenite solution (containing 5.16 x 10^{-15} mol of Se) were filled into the glass tubes. Afterwards the pH was adjusted and 100 mg LDH was added. The samples were stored for two days before sampling (described above).

Results

From the ICP-OES measurements a Mg/Cd/Al mole ratio of 2.91:0.09:1 for the Mg-Cd-Al LDH was calculated. These results show that a 3:1 LDH-type in respect of the ratio of divalent and trivalent cations was synthesized. The empirical formula of the Mg-Cd-Al LDH was derived as $[Mg_{2.91}Cd_{0.09}Al(OH)_8]Cl_{0.98}(CO_3)_{0.01} \cdot 1.91H_2O$. The amount of the interlayer water was obtained by DTA-TGA analysis. To calculate the theoretical anion exchange capacity (TAEC) from the empirical formula the presence of carbonate in the interlayer was ignored. The TAEC for monovalent anions is 3.12 x 10^{-3} mol/g, which means that at most 3.12 x 10^{-3} mol/g chloride can be exchanged by other monovalent anions. For divalent anions it is reduced to 1.56 x 10^{-3} mol/g.

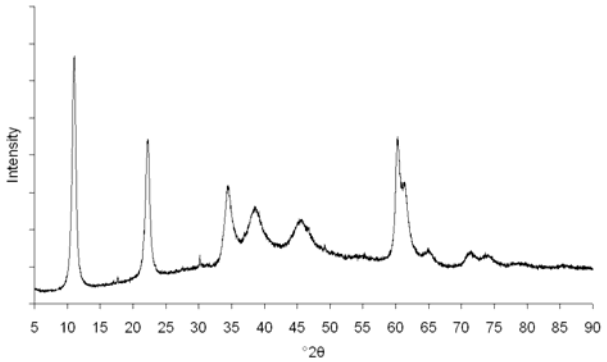

Fig. 1: XRD pattern of the Mg-Cd-Al LDH

For the synthesized Mg-Cd-Al LDH X-ray diffraction measurements were performed. In the XRD pattern obtained symmetric 00*l* basal reflections were cognizable (Figure 1). The very broad and asymmetric reflections in the range of 32-55°2θ indicated a highly disordered structure. This structure was described by Curtius and Ufer [15] as a mixture of the trigonal $3R_1$ polytype with rhombohedral symmetry and the hexagonal $2H_1$ polytype which have a different *c* spacing. At 17.7°2θ and 30.2°2θ two additional peaks were present. These peaks could be assigned to $Cd(OH)_2$. A quantification of the amount of this impurity by an internal standard as described by Curtius and Ufer [15] was performed and showed that the Mg-Cd-Al LDH contained 0.3-0.4 wt% of $Cd(OH)_2$. This was only a minor amount of cadmium hydroxide. Due to the fact that no other by-products were observed nearly all of the cadmium could only be incorporated. Using the basal reflection at 11.1°2θ the spacing of the layers was calculated to be 7.998 Å and from the *hk*0-reflection (110) at 60.3°2θ the *a* lattice parameter was calculated to be a = 3.067 Å. These values agreed with the values of Mg-Al LDHs found in literature [4].

The IR spectrum showed strong hydroxyl and water stretching and bending bands at 3484 cm^{-1} and 1630 cm^{-1}. In the region from 1100 to 500 cm^{-1} appeared Al-O and Mg-O vibration bands as well as Al-O bending bands. A weak stretching band due to adsorbed CO_3^{2-} was present at 1371 cm^{-1}. This carbonate was only caused by the KBr pellet preparation and not by the synthesis. This assumption could be confirmed by an IR measurement directly after synthesis and dialysis of the Mg-Cd-Al LDH by single reflection diamond attenuated total reflection (ATR) where no carbonate was observed.

For the Mg-Cd-Al LDH a specific surface area of 46 m^2/g was determined by BET. After treatment of the solid with the ammonium carbonate solution only traces of Cd were released. Considering the error range of element analysis by ICP-OES the molar stoichiometry of the Mg-Cd-Al LDH did not change in relation to Mg, Cd and Al. Due to the fact that the leaching with ammonium carbonate solution did not remove coprecipitated elements [16] it could be assumed that nearly all of the Cd was incorporated. The released traces of Cd agreed with the observed impurity by XRD measurement.

During the time-dependent sorption investigations of selenite on the Mg-Cd-Al LDH in water (10 g/L), equilibrium was reached in less than one hour (Figure 2). Selenite adsorbed quantitatively. This corresponds to an anion exchange capacity of 1.12 x 10^{-14} mol/g. The equilibrium pH was 6.78 (± 0.16). In clay pore water selenite sorbed up to 62 % according to an anion exchange capacity of 6.94 x 10^{-15} mol/g. The equilibrium pH was 6.52 (± 0.25). The selenite sorption in brine 2 reached a value of 23 % at an equilibrium pH of 6.26 (± 0.02). The sorption corresponds to an anion exchange capacity of 2.58 x 10^{-15} mol/g. At investigations of the sorption on a Mg-Al LDH from Curtius *et al.* the selenite sorption in clay pore water reached a value of 55 % and in brine 2 the selenite sorbed up to 20 %. The pH values were comparable. These results showed that the Mg-Al LDH containing Cd had a better sorption capacity than the Mg-Al LDH.

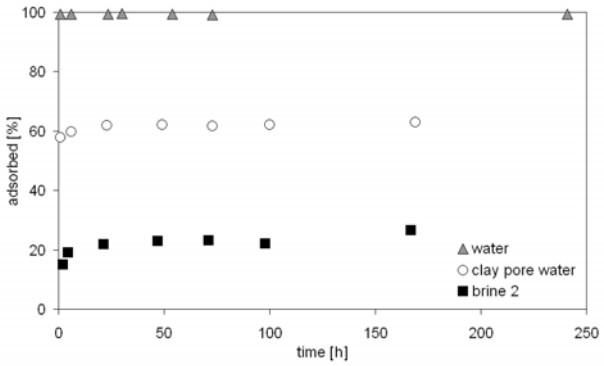

Fig. 2: Sorption kinetics of selenite on the Mg-Cd-Al LDH in water, clay pore water and brine 2.

The selenite sorption decreased in the sequence water, clay pore water and brine 2 which could be explained by the increasing amount of chloride as a competing anion in the solutions. This dependency on the ionic strength indicated that the sorption mechanism is an ion exchange process and no chemical adsorption. Curtius *et al.* [13] described the same observations at their investigations of the sorption of selenite on a Mg-Al LDH and on a Mg-Al-Eu LDH. The ion exchange capacities of the LDHs were reduced by the high chloride concentration as competing anions. Compared to the used selenite concentration the chloride anions represented a molar excess of approximately 5.4 x 10^{11} in clay pore water and approximately 1.8 x 10^{13} in brine 2. Therefore the sorption in water was quantitatively. Due to the discovery of Miyata [3] that the selectivity in the exchange reaction increased with increasing anion charge density the sorption of selenite is possible in spite of the high chloride concentrations.

To investigate the influence of pH on sorption of selenite the initial pH was adjusted between 3.5 and 8 at water and clay pore water and between 3.5 and 6 at brine 2 (Figure 3). The obtained equilibrium pH in water was 6.61 (± 0.46), in clay pore water 5.81 (± 0.12) and in brine 2 6.23 (± 0.03). A comparison of these initial and equilibrium pH values showed that the Mg-Cd-Al LDH must have a high pH buffering capacity and the sorption of selenite does not depend on pH in the investigated initial pH ranges.

During the desorption studies no selenite desorbed in water. In clay pore water and in brine 2 selenite desorbed continuous in the course of the investigations. The de-

sorption rate in clay pore water represented approximately 2 % in each case; in brine 2 it averaged approximately 10 %. No equilibrium was reached in the observed time period and therefore no statement could be made whether the selenium will be desorbed completely over the years.

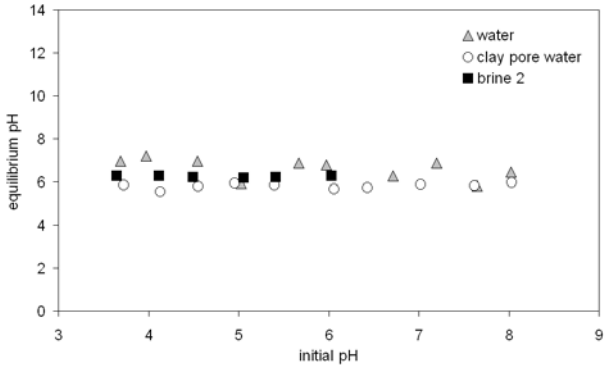

Fig. 3: pH dependency on the sorption of selenite on the Mg-Cd-Al LDH in water, clay pore water and brine 2.

To obtain the adsorption isotherms the amount of selenite sorbed on the Mg-Cd-Al LDH, C_{ads}, was plotted against the equilibrium selenite concentration, C_e, in clay pore water and in brine 2 (Figure 4). The pH averaged 5.99 (± 0.24) in clay pore water and 6.28 (± 0.05) in brine 2. In the concentration range used no saturation was reached because the adsorption isotherms were both linear. Châtelet *et al.* [17] described that this behaviour indicates an exchange mechanism, in which the possible adsorption sites in LDHs are located within the interlayer.

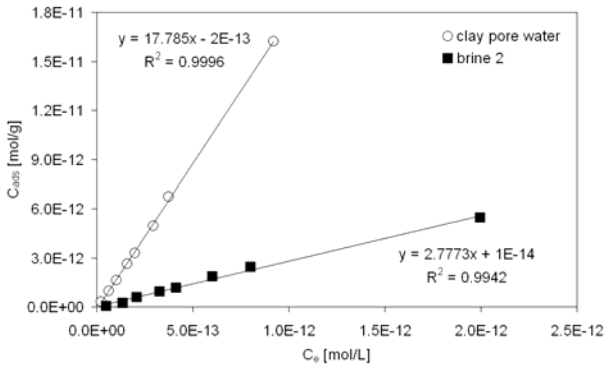

Fig. 4: Isotherms of selenite sorption on the Mg-Cd-Al LDH in clay pore water and brine 2.

The sorption data were furthermore analyzed in terms of the Freundlich equation. The fitting gave linear isotherms with slopes of about one which indicates that a concentration-independent adsorption of selenite in clay pore water and brine 2 exists in the concentration range used [13]. As an alternative to the Freundlich isotherm, the data were fitted to the Dubinin-Radushkevich (D-R) equation [18]:

$$X = X_m \exp(-K\varepsilon^2), \quad (1)$$

in which X is the amount of solute adsorbed per unit weight of solid (mol/g), X_m the maximum sorption capacity of adsorbent per unit weight (mol/g), ε the Polanyi potential = $RT \ln(1+1/C_e)$, R the gas constant (kJ/K mol), C_e the equilibrium concentration of solute in solution (mol/L), T the temperature (K) and K the constant related to the sorption energy (mol^2/kJ^2).

The mean energy of sorption, E, is the free energy change when one mol of ion is transferred to the surface of the solid from infinity in the solution, and it is calculated from:

$$E = (-2K)^{-1/2}. \quad (2)$$

The D-R equations gave also satisfactory fits to the obtained results (R^2 = 0.9997 for clay pore water and R^2 = 0.9819 for brine 2, Figure 5). In clay pore water the mean energy of the sorption was calculated to be 12.9 kJ/mol and in brine 2 it was 11.8 kJ/mol. These values lay in the range of ion exchange processes [19]. The maximum sorption capacities (X_m) were obtained from the intercept points of the functions with the ordinate. X_m in clay pore water was found to be 2.37 x 10^{-5} mol/g and in brine 2 it was 6.27 x 10^{-5} mol/g. These values were significant lower than the TAEC for divalent anions (1.56 x 10^{-3} mol/g). One reason could be the high amount of chloride in the solutions whereby the ion exchange processes could only take place at the edges of the interlayer of the Mg-Cd-Al LDH.

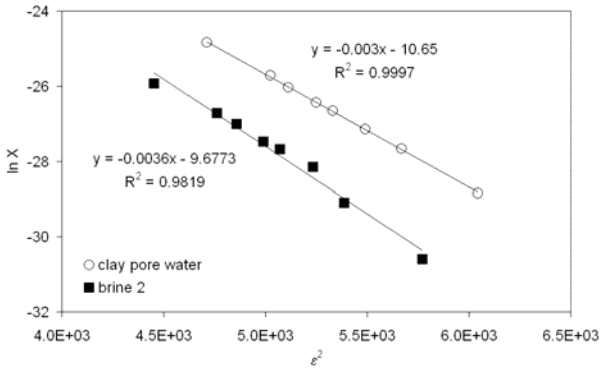

Fig. 5: D-R plots of selenite sorption on the Mg-Cd-Al LDH in clay pore water and brine 2.

Conclusions

The present investigations were performed to study the incorporation behavior of cadmium into the lattice structure of a Mg-Al LDH with chloride in the interlayer. A Mg-Cd-Al LDH in which 3.3 % of the molar amount of

Mg was exchanged by Cd should be synthesized *via* co-precipitation. From the chemical analysis the formula $[Mg_{2.91}Cd_{0.09}Al(OH)_8]Cl_{0.98}(CO_3)_{0.01} \cdot 1.91H_2O$ was derived.

During the XRD measurements of the Mg-Cd-Al LDH only minor amounts of $Cd(OH)_2$ were quantified. From this determination was inferred that nearly all of the cadmium could only be incorporated because no other by-products were observed. The values for the spacing of the layers and the *a* lattice parameter was calculated. They agreed with values of other Mg-Al LDHs found in literature. After treatment of the solid with an ammonium carbonate solution the molar ratio did not change considering the error range of element analysis by ICP-OES. This could be another indication for incorporation of Cd. The mentioned indications argue on the basis of the investigations for the incorporation of cadmium into the lattice structure of the Mg-Al LDH. But due to the differences in the crystal chemical properties of Mg and Cd, for example the ionic radii, the incorporation can not be attested completely up to now. In future, extended X-ray absorption fine structure (EXAFS) investigations in order to determine the coordination sphere of Cd will be performed.
The sorption behaviour of selenite on the Mg-Cd-Al LDH was investigated in water, clay pore water and brine 2. Time-dependent and isotherm studies as well as the influence of pH and competing anions were performed. The time-dependent investigations showed that the sorption of selenite in water, clay pore water and brine 2 was very fast and the equilibrium in water was reached in less than one hour. In clay pore water and brine 2 the equilibrium was reached within a half day. In comparison to results of selenite sorption on a Mg-Al LDH from Curtius *et al.* the Mg-Cd-Al LDH showed a better sorption capacity. Under final disposal conditions the formation of a Mg-Cd-Al LDH could not be excluded. This LDH-type is more effective than the Mg-Al LDH with respect to the retardation of selenite.

During the desorption investigations in water no release of selenite was observed. In clay pore water and in brine 2 selenite desorbed continuously in the course of the observed time period. For the investigations of the effect of pH on selenium sorption the obtained equilibrium pH in water was 6.61 (± 0.46) and in clay pore water 5.81 (± 0.12). In brine 2 the resulting equilibrium pH was 6.23 (± 0.03). These results demonstrated the high buffer capacity of the Mg-Cd-Al LDH.

The adsorption isotherms were all linear. The sorption energies were calculated and they lay in the range of ion exchange processes. The sorption of selenite decreased with increasing concentration of the competing chloride anions in the used solutions. This dependency on the ionic strength is also an indication for the fact that the sorption mechanism is an ion exchange process.

Due to the results of the sorption investigations the Mg-Cd-Al LDH will be able to retard selenite in spite of the high molar chloride excess in consideration of the final disposal in clay or salt.

Outlook

These studies are only based on the sorption of selenite on a Mg-Cd-Al LDH. In a possible repository a multiplicity of radionuclides would be released during the corrosion of the spent research reactor fuel elements. Hence sorption investigations on the Mg-Cd-Al LDH should be performed with other long term safety-relevant ions mainly because of the expected better sorption capacity in comparison to a Mg-Al LDH.

References

[1] Curtius, H., et al., *Untersuchungen zum Verhalten von Forschungsreaktor-Brennelementen (FR-BE) in den Wirtsgesteinsformationswässern möglicher Endläger*, Berichte des Forschungszentrums Jülich, 4237, ISSN 0944-2952 (2006).

[2] Reichle, W.T., *Synthesis of anionic clay minerals (mixed metal hydroxides, hydrotalcite)*, Solid States Ionics, **22**, 135-141 (1986).

[3] Miyata, S., *Anion-exchange properties of hydrotalcite-like compounds*, Clays and Clay Minerals, **31**, 305-311 (1983).

[4] Miyata, S., *The synthesis of hydrotalcite-like compounds and their structures and physico-chemical properties - I: The systems Mg^{2+}-Al^{3+}-NO_3^-, Mg^{2+}-Al^{3+}-Cl^-, Mg^{2+}-Al^{3+}-ClO_4^-, Ni^{2+}-Al^{3+}-Cl^- and Zn^{2+}-Al^{3+}-Cl^-*, Clays and Clay Minerals, **23**, 369-375 (1975).

[5] Cavani, F., Trifirò, F., Vaccari, A., *Hydrotalcite-type anionic clays: preparation, properties and applications*, Catalysis Today, **11**, 173-301 (1991).

[6] Miyata, S., Kumura, T., *Synthesis of new hydrotalcite-like compounds and their physico-chemical properties*, Chemistry Letters, 843-848 (1973).

[7] Vichi, F.M., Alves, O.L., *Preparation of Cd/Al layered double hydroxides and their intercalation reactions with phosphonic acids*, Journal of Materials Chemistry, **7**, 1631-1634 (1997).

[8] Shannon, R.D., *Revised effective ionic radii and systematic studies of interatomic distances in halides and chalcogenides*, Acta Crystallographica, A **32**, 751-767 (1976).

[9] Das, J., et al., *Studies on Mg/Fe hydrotalcite-like-compound (HTlc) - I. Removal of inorganic selenite (SeO_3^{2-}) from aqueous medium*, Journal of Colloid and Interface Science, **251**, 26-32 (2002).

[10] Das, N.N., et al., *Adsorption of Cr(VI) and Se(IV) from their aqueous solutions onto Zr^{4+}-substituted ZnAl/MgAl-layered double hydroxides: effect of Zr^{4+} substitution in the layer*, Journal of Colloid and Interface Science, **270**, 1-8 (2004).

[11] You, Y., Vance, G.F., Zhao, H., *Selenium adsorption on Mg-Al and Zn-Al layered double hydroxides*, Applied Clay Science, **20**, 13-25 (2001).

[12] Yang, L., et al., *Removal of trace levels of arsenic and selenium from aqueous solutions by calcined and uncalcined layered double hydroxides (LDH)*, Industrial & Engineering Chemistry Research, **44**, 6804-6815 (2005).

[13] Curtius, H., Paparigas, Z., Kaiser, G., *Sorption of selenium on Mg-Al and Mg-Al-Eu layered double hydroxides*, Radiochimica Acta, **96**, 651-655 (2008).

[14] Weiss, A., Toth, E., *Untersuchungen zur Synthese, Quellungseigenschaften und Anionenaustausch von kristallchemisch modifizierten Doppelhydroxiden vom Hydrotalkit-Typ*. Wolf, D., Starke, R., Kleeberg, R. (Ed.), Contributions of the annual DTTG meeting Freiberg, 267-276 (1996). ISSN 1432-7007, online available at http://www.dttg.ethz.ch/band4_en.html.

[15] Curtius, H., Ufer, K., *Eu incorporation behavior of a Mg-Al-Cl layered double hydroxide*, Clays and Clay Minerals, **55**, 354-360 (2007).

[16] Duff, M.C., Coughlin, J.U., Hunter, D.B., *Uranium co-precipitation with iron oxide minerals*, Geochimica et Cosmochimica Acta, **66**, 3533-3547 (2002).

[17] Châtelet, L., et al., *Competition between monovalent and divalent anions for calcined and uncalcined hydrotalcite: anion exchange and adsorption sites*, Colloids and surfaces, A: Physicochemical and Engineering Aspects, **111**, 167-175 (1996).

[18] Atun, G., Bilgin, B., Mardinli, A., *Sorption of cesium on montmorillonite and effects of salt concentration*, Journal of Radioanalytical and Nuclear Chemistry, Articles, **211**, 435-442 (1996).

[19] Khan, S.A., Reman, R.-U., Khan, M.A., *Adsorption of Cs(I), Sr(II) and Co(II) on Al_2O_3*, Journal of Radioanalytical and Nuclear Chemistry, Articles, **190**, 81-96 (1995).